

We are IntechOpen, the world's leading publisher of Open Access books Built by scientists, for scientists

6,900

Open access books available

186,000

International authors and editors

200M

Downloads

Our authors are among the

154

Countries delivered to

TOP 1%

most cited scientists

12.2%

Contributors from top 500 universities



WEB OF SCIENCE™

Selection of our books indexed in the Book Citation Index
in Web of Science™ Core Collection (BKCI)

Interested in publishing with us?
Contact book.department@intechopen.com

Numbers displayed above are based on latest data collected.
For more information visit www.intechopen.com



Laser-Induced Fluorescence of Hydroxyl (OH) Radical in Cold Atmospheric Discharges

Jan Voráč, Pavel Dvořák and Martina Mrkvičková

Additional information is available at the end of the chapter

<http://dx.doi.org/10.5772/intechopen.72274>

Abstract

The application of laser-induced fluorescence (LIF) to measurement of absolute concentration of hydroxyl radicals in cold atmospheric discharges is described. Though only the case of OH is presented, the method can be directly applied to other molecules as well. Starting from the rate equations for the LIF process, the main formulas for two- and multi-level excitation scheme are derived. It is also shown how to use partially saturated LIF in practice, enhancing the signal-to-noise ratio. Practical tips for automating the data evaluation are given, allowing processing large data sets, particularly suitable for planar measurements. Gas temperature estimation from fluorescence on different rotational absorption lines is shown as an attractive method for obtaining temperature maps with high spatial resolution. The important aspects of calibration are discussed, particularly the overlap of the laser line with the selected absorption line and the measurement of the Rayleigh scattering for sensitivity calibration, together with the common sources of errors. The application of OH(A, $v' = 0 \leftarrow X, v'' = 0$) excitation scheme to the effluent of atmospheric pressure plasma jet ignited in argon and of OH(A, $v' = 1 \leftarrow X, v'' = 0$) to the plasma of coplanar surface barrier discharge in air and in water vapor is shown.

Keywords: laser-induced fluorescence, atmospheric pressure plasma, hydroxyl, concentration, spectroscopy

1. Introduction

Even though the hydroxyl (OH) in laboratory discharges readily emits radiation, which may be the source of many interesting information [1], there is no known direct and reliable method of determining the total OH radical density from the emission spectra. Indeed, the radicals in the ground electronic states are usually the most abundant and their effect on the plasma chemistry is dominant, but they are not observable by simple emission spectroscopy. Absorption-based

spectroscopic techniques allow access directly to the ground electronic states. In absorption spectroscopy, the decrease in the light intensity after passing through the probed volume is observed. The information obtained by absorption spectroscopy is thus line-integrated. On the other hand, the evaluation of the measurement is quite straightforward and absorption measurements could be considered less vulnerable to errors compared to fluorescence measurements. The sensitivity of absorption spectroscopy for single pass may be insufficient for some laboratory discharges and multi-pass cells need to be constructed, complicating the experiment and the data evaluation.

Laser-induced fluorescence (LIF) is an interesting combination of absorption and emission spectroscopy. It is naturally more complicated than either of these methods alone, both experimentally and theoretically. In return, it offers higher sensitivity compared to single-pass absorption measurements, good spatial resolution given by intersection of the laser beam, and the optical path of observation. To obtain the absolute concentration, many things need to be taken into account and there are many partial measurements that need to be done and evaluated. In this chapter, we show how the OH fluorescence measurements in atmospheric pressure discharges can be performed, including tricks that can be applied for conditions with low ratios of wanted-to-unwanted signals. We shall also show what information may be extracted from the partial steps that are necessary for the concentration determination.

Hydroxyl is a diatomic radical consisting of an oxygen and a hydrogen atom. It contains an unpaired electron, which makes it a highly reactive species—its lifetime in an open atmosphere is typically less than a second [2]. It can bind to a polymer surface, forming a functional group and increasing its wettability [3]. It has been proved that introducing OH radicals into mixtures containing volatile organic compounds leads to removal of these pollutants, for example, [4]. It has also been found that the OH radical plays an important role in the response of immune system to infection [5–7]. OH radical radiation on the $A^2\Sigma^+ \rightarrow X^2\Pi$ electronic transition with the strongest band in the near UV at 306 nm is also readily present in nearly all laboratory discharges, as the water impurities are notoriously difficult to avoid and the water molecule is easily dissociated, forming an OH radical. Part of the dissociation products is created directly in the excited $A^2\Sigma$ electronic state. This is responsible for a considerable amount of UV radiation also in plasma jets used for plasma medicine, introducing another mean of affecting both the patient's tissue and the eventual invading microorganisms.

Consequently, OH has been intensively spectroscopically studied. The fundamental work of Dieke and Crosswhite [8] offered a good description of the quantum states with satisfactorily precise values necessary for the energy levels calculation. Luque and Crosley later added calculations for transition probabilities [9]. Together with improved calculations of energy levels, this has already been sufficient for precise simulations of the molecular spectrum as available in their free software LIFBASE [10].

2. Structure of OH radical and its spectrum

In this section, we briefly summarize the structure of the OH radical focusing on how it affects its spectrum. For details, see the comprehensive book of Herzberg and Spinks [11].

Symbol	Meaning
J	Total angular momentum
N (K in [11])	Total angular momentum apart from the electronic spin
S	Angular momentum of electronic spin

Table 1. List of quantum numbers used in this chapter and their meaning.

The two most relevant electronic states for OH spectroscopy are the ground state X $^2\Pi$ and the first excited state A $^2\Sigma^+$, in further text we call them briefly X and A. They are approximately 4 eV apart. This energy gap corresponds to photon wavelengths around 300 nm. Both mentioned electronic states have resulting spin 1/2 and are thus doublets.

The ground electronic state is a Π state, that is, the resulting length Λ of the projection of the electronic orbital angular momentum to the internuclear axis is 1. For lower rotational states, the dominant fine-structure-splitting mechanism is the spin-orbit coupling. However, for

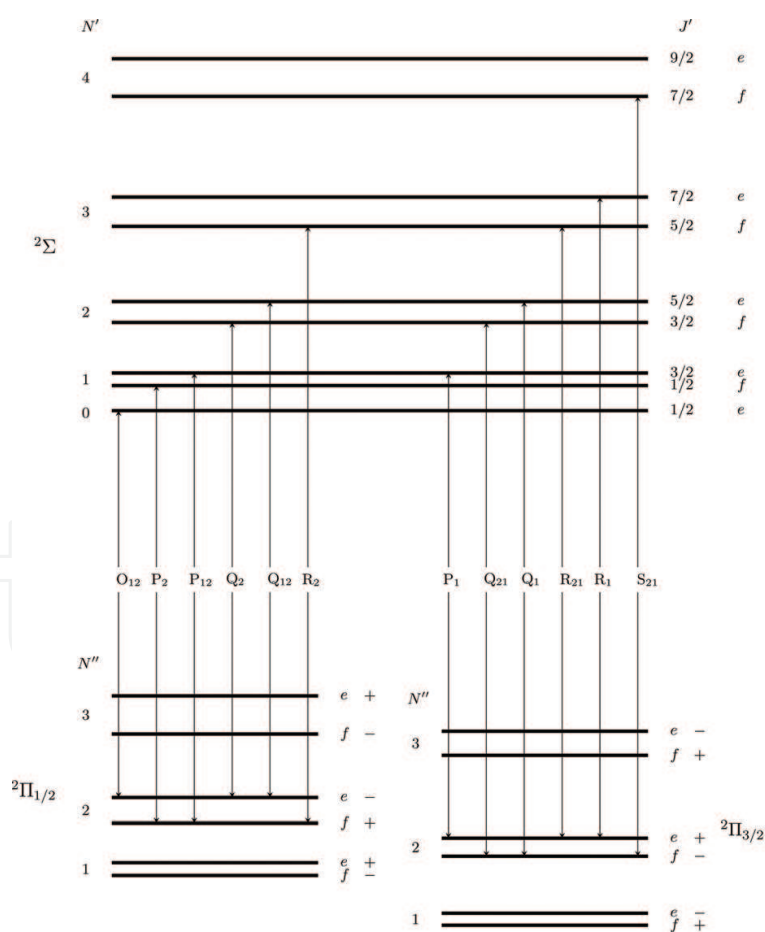


Figure 1. Diagram of $^2\Sigma \leftrightarrow ^2\Pi$ transitions. The J values are omitted for the $^2\Pi$ state. It would be $J = N - 1/2$ for the $^2\Pi_{1/2}$ state and $J = N + 1/2$ for the $^2\Pi_{3/2}$. The lines are labeled according to Hund's case (b), that is, P for $\Delta N = -1$, Q for $\Delta N = 0$ and R for $\Delta N = 1$. Note that the Π states do not have $N = 0$.

higher rotational states the spin-rotational coupling starts to gain importance and for $J \geq 8.5$ starts to dominate. The ground electronic state is thus an intermediate state between Hund's cases (a) and (b). Consequently, neither the N nor the J quantum number is considered "good," but both are "almost good" and can be used to label the rotational states depending on the preference.¹ The relation between the two is $J = N \pm 1/2$ for the fine-structure components, usually labeled 1 and 2, respectively. See **Table 1** for summary of the quantum numbers. The Λ -doubling effect is also present. Effectively, there are always four different states with the same vibrational and rotational excitation—two orientations of the electronic spin (spin-orbit and spin-rotational splitting) and two orientations of the projection of total orbital momentum of electrons to the internuclear axis. Due to symmetry selection rules (only $+$ \leftrightarrow $-$ transitions are allowed), only one of the two Λ -doublet components is available for the photon absorption. This is important to take into account when calculating the radical concentration from the LIF measurements. The \pm parity is derived from the (anti)symmetry of the wavefunction with respect to mirroring by an arbitrary plane containing the internuclear axis. Because this property switches with the rotational quantum number, a notation e, f was introduced as $\begin{pmatrix} e \\ f \end{pmatrix} = \pm(-1)^{J-1/2}$, see **Figure 1**.

The first excited state A is a Σ state, that is, $\Lambda = 0$. Σ electronic states are best described by Hund's case (b), the good quantum number for rotational state is N . There is no spin-orbit coupling and no Λ -doubling effect. The fine-structure splitting happens solely due to spin-rotational interaction. In this case, the energy spacing of the doublet levels is given by $\gamma(N + 1/2)$, that is, increases linearly with rotational quantum number. The energy splitting of the doublet components is smaller compared to the X $^2\Pi$ state.

The structure of the OH energy levels is sketched in **Figures 1–3**. The A $^2\Sigma$ state is affected by the spin-rotation interaction which causes a splitting of each rotational state into two sublevels. Similarly, the X $^2\Pi$ state is affected dominantly by the spin-orbit interaction. Each of these two effects causes doubling of each expected rotational line, so we have four lines for $\Delta J = -1$, four lines for $\Delta J = 0$, and four other lines for $\Delta J = +1$. This makes 12 lines altogether. The Λ -doubling of the $^2\Pi$ state, on the other hand, introduces no further splitting of the observed rotational lines. This is because of the $+$ \leftrightarrow $-$ parity selection rule. Because of the Λ -doubling, the Q(N'') lines have different lower state than P(N'') or R(N'') lines. Here, we have used the standard spectroscopic abbreviation: single prime (N') is used to describe the upper state of a transition (here exclusively the electronic state A) and double prime (N'') describes the lower state (here exclusively the X electronic state).

¹In this text, we adopt the newer notation with J for the quantum number describing the total angular momentum (apart from the nuclear spin that will be neglected in the whole chapter), N for the total angular momentum *apart from the electronic spin*, R for pure rotation (seldom used), and S for angular momentum of electronic spin, as in [12, 13]. In Herzberg's book, the same quantum numbers are called $J, K, N,$ and $S,$ respectively.

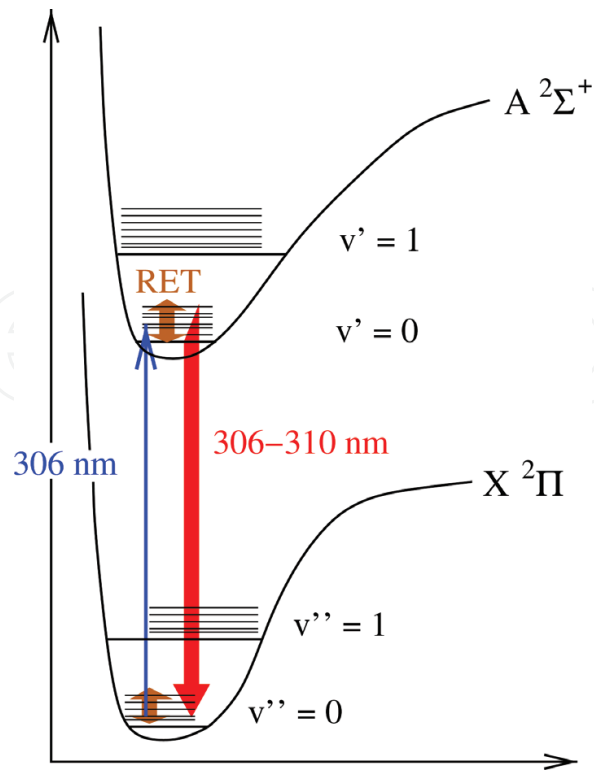


Figure 2. Fluorescence schema of the excitation to the $v' = 0$ state of OH radicals.

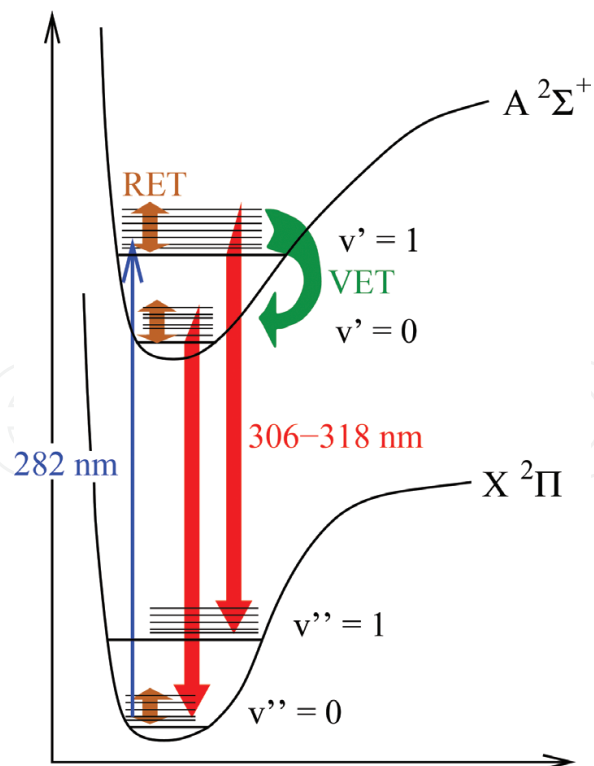


Figure 3. Fluorescence schema of the excitation to the $v' = 1$ state of OH radicals.

3. Excitation schema

Although only one specific rotational level can be excited by laser with narrow spectral linewidth, collisional processes can change both vibrational and rotational state of the excited molecular species. As a result, the fluorescence spectrum of OH radicals usually consists of numerous rotational lines that are merged to several vibrational bands. The composition of fluorescence spectrum depends markedly on particular vibrational state that is excited by laser:

1. The simplest situation is realized when OH radicals are excited to the ground vibrational state $A^2\Sigma^+(v' = 0)$ [14]. When no thermal excitation to higher vibrational states occurs, the only intensive fluorescence radiation is the 0 – 0 vibrational band located between 306 and 314 nm. Other vibrational bands originating from the ground vibrational state are weak due to their low Franck-Condon factors. Since excitation and fluorescence wavelengths coincide, the fluorescence signal cannot be separated from scattered laser radiation spectrally. Consequently, this excitation schema can be used for LIF experiments only when temporal separation can be used, that is, when the lifetime of the excited OH state is longer than the laser pulse duration and the fluorescence signal can be detected after the end of the laser pulse.
2. The spectral separation is simply achieved when OH radicals are excited to the first vibrationally excited state $A^2\Sigma^+(v' = 1)$ [15–18]. In this case, excitation wavelengths around 282 nm are used. Fluorescence vibrational bands 1 – 1 (312–320 nm) and 0 – 0 (306–314 nm) are usually used for detection, which can be separated from scattered excitation radiation by spectral filters. The 0 – 0 vibrational band arises due to the collisional vibrational energy transfer (VET) and its intensity depends on the ratio between the VET rate and the total deexcitation rate of the $(v' = 1)$ state.
3. Alternatively, higher vibrational states can be excited as well. In these cases, the kinetics of excited states is even more complicated. Excitation to the $A^2\Sigma^+(v' = 3)$ state is sometimes used, since this state undergoes rapid predissociation, which reduces the dependence of excitation state lifetime on collisional quenching [19]. On the other hand, the dissociation reduces the fluorescence signal, and the influence of collisional processes on the lifetime of excited OH radicals is not entirely avoided, especially at high pressure. That is why we further concentrate only on excitation to the $v' = 0$ and $v' = 1$ state.

The vibrational and rotational distribution of the excited state should be taken into account during processing of measured data, since rovibrational levels differ in fluorescence quantum yield and wavelengths. Consequently, the sensitivity of the method depends on the rovibrational distribution. The intensity of the measured fluorescence signal can be expressed as the sum of contributions from all spectral lines generated by the excited OH radical

$$M_f = \iiint_V \frac{\Omega}{4\pi} \int_0^\infty \sum_{v''} \sum_{j''} \sum_{\alpha''} F(\lambda_{v''j''\alpha''}^{v'j'\alpha'}) D(\lambda_{v''j''\alpha''}^{v'j'\alpha'}) A_{v''j''\alpha''}^{v'j'\alpha'} N^{v'j'\alpha'} dt dV \quad (1)$$

with the following meaning of used symbols: Ω is the solid angle in which the fluorescence is collected by the detector, F is the transmittance of optics in front of the detector (usually the

transmittance of an interference filter), D is the detector sensitivity, A is the emission coefficient for the particular line, and N is the concentration of excited OH radical in the particular level described by vibrational number v' , total angular momentum number J' , and doublet component α' . (The doublet component can have two values, usually labeled as 1 and 2.) λ is the wavelength of the particular line. The signal is integrated over the whole detection volume and the whole time of the detection process. The absolute detector sensitivity is usually not known and needs to be calibrated. However, the relative dependence of the sensitivity is simply achievable. Therefore, we describe the detector sensitivity as a product $D = D_a \cdot d$ of a known function of wavelength $d(\lambda)$ and an unknown constant D_a .

Concentration of all excited levels involved in the fluorescence process can be calculated by means of a set of tens kinetic equations. Luckily, at atmospheric pressure the rotational equilibrium of each particular vibronic $A^2\Sigma^+$ state is often reached quickly, which can be used for a considerable simplification of Eq. (1). In this simplification, we describe the relative population of each rotational level by the Boltzmann factor

$$f_{v'J'\alpha'} = \frac{(2J' + 1)\exp\left(-\frac{E_{v'J'\alpha'}}{kT}\right)}{\sum_{J'\alpha'} (2J' + 1)\exp\left(-\frac{E_{v'J'\alpha'}}{kT}\right)} \quad (2)$$

and we assume that saturation effects are negligible. At these assumptions, the kinetic equations of the fluorescence process enable to express the fluorescence signal by

$$M_f = N_{Xi} \frac{\kappa B}{c} E_f \tau_1 \left[\sum_{J''\alpha''} F\left(\lambda_{v''=1J''\alpha''}^{v'=1J'\alpha'}\right) d\left(\lambda_{v''=1J''\alpha''}^{v'=1J'\alpha'}\right) A_{v''=1J''\alpha''}^{v'=1J'\alpha'} f_{v''=1J''\alpha''}(T) + \right. \\ \left. + V\tau_0 \sum_{J''\alpha''} F\left(\lambda_{v''=0J''\alpha''}^{v'=0J'\alpha'}\right) d\left(\lambda_{v''=0J''\alpha''}^{v'=0J'\alpha'}\right) A_{v''=0J''\alpha''}^{v'=0J'\alpha'} f_{v''=0J''\alpha''}(T) \right] \iiint_V D_a \frac{\Omega}{4\pi} s dV. \quad (3)$$

for excitation to the $v' = 1$ state and detection of 1 – 1 and 0 – 0 vibrational bands and by

$$M_f = N_{Xi} \frac{\kappa B}{c} E_f \tau_0 \left[\sum_{J''\alpha''} F\left(\lambda_{v''=0J''\alpha''}^{v'=0J'\alpha'}\right) d\left(\lambda_{v''=0J''\alpha''}^{v'=0J'\alpha'}\right) A_{v''=0J''\alpha''}^{v'=0J'\alpha'} f_{v''=0J''\alpha''}(T) \right] \iiint_V D_a \frac{\Omega}{4\pi} s dV. \quad (4)$$

for excitation to the $v' = 0$ state. N_{Xi} denotes the concentration of OH radicals in the particular rotational level of the ground vibronic state $X^2\Pi(v'' = 0)$ from which the excitation occurred, B is the absorption coefficient of the particular excitation transition, c is the speed of light and κ is the overlap term of the absorption and laser line [20], E_f is the mean energy of laser pulses during the measurement of the fluorescence, τ is the lifetime of the relevant vibronic state, and V is the $A^2\Sigma^+(v' = 1) \rightarrow A^2\Sigma^+(v' = 0)$ VET rate constant. The spatial laser beam profile s is proportional to the area density of laser energy and it is normalized to one when integrated in the plane perpendicular to the laser beam direction, that is, $\iint_s s dS = 1$. The value of the integral $\iiint_V D_a \frac{\Omega}{4\pi} s dV$ can be calibrated by means of Rayleigh scattering, see Section 9.

Eqs. (3) or (4) can be used for the calculation of OH concentration in the ground state. Since N_{X_i} includes only OH radicals in one particular rotational level, it is necessary to calculate the concentration of all OH radicals in the ground vibronic state $X^2\Pi(v'' = 0)$ by means of the Boltzmann factor

$$N_X = N_{X_i}/f_{X_i} = N_{X_i} \frac{2 \sum_j (2J_j + 1) \exp\left(-\frac{E_j}{kT}\right)}{(2J_i + 1) \exp\left(-\frac{E_i}{kT}\right)}. \quad (5)$$

Factor 2 in the numerator is caused by the Λ -doubling.

4. Instrumentation

For a typical state-of-art LIF experiment, an extensive instrumentation is necessary. An example of such setup for a point like or line-resolved measurement is shown in **Figure 4** and the necessary beam expansion optics for a planar LIF imaging is in **Figure 5**.

The core instrument of every LIF experiment is a laser system tunable in wavelength. The power source of such laser system is usually a powerful pulsed laser, typically Nd:YAG. Its frequency-doubled (532 nm) or -tripled (355 nm) output is used to pump a wavelength-tunable light source, typically a dye laser with a movable dispersive element in the cavity to control the resonance wavelength. The tuning range of dye lasers is limited by the available dyes, but can be greatly enhanced by using nonlinear frequency conversion. This way, visible light (typically in the range of 556–662 nm for the well-behaving family of rhodamine dyes) can be converted to as low as 200 nm.

Alternatively, solid-state optical parameter oscillator (OPO)-tunable lasers can be used, but despite the noticeable recent advances in this technology, dye lasers with frequency conversion

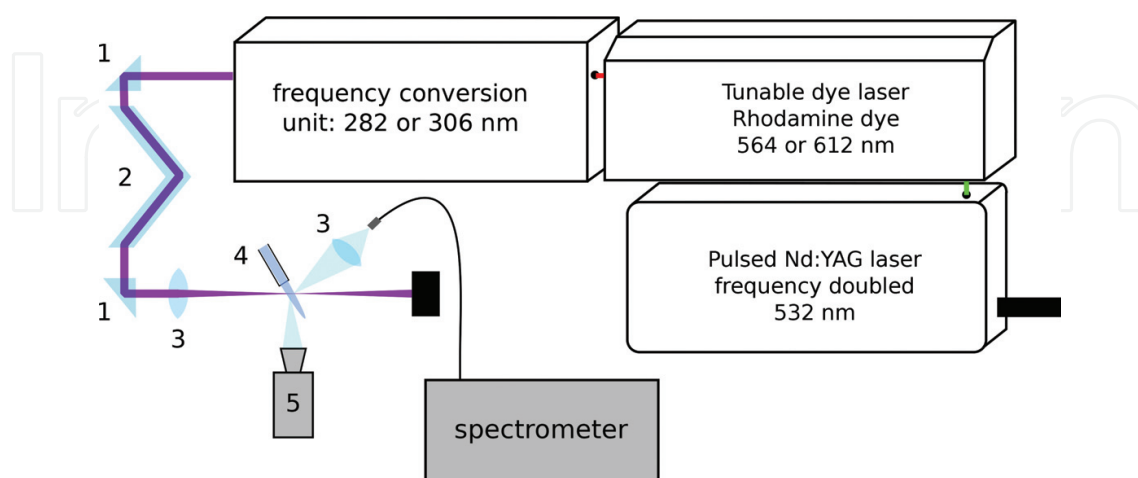


Figure 4. Instrumentation of an LIF experiment. 1 – Right-angle prism, 2 – Fresnel rhomb tandem to turn polarization (only, if necessary), 3 – Spherical positive UV lens, 4 – Investigated plasma source, 5 – ICCD camera synchronized with the laser.

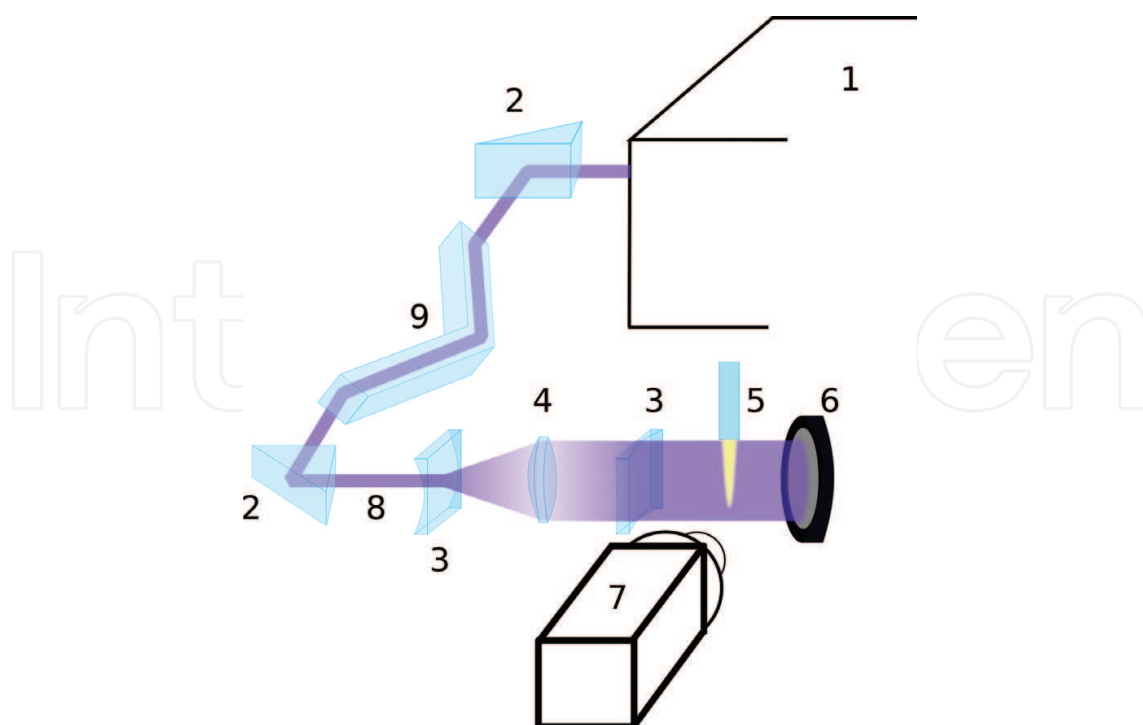


Figure 5. Instrumentation of a planar LIF experiment. 1 – Pulsed tunable laser, 2 – Right-angle prism, 3 – Cylindrical negative UV lens, 4 – Spherical positive UV lens, 5 – Investigated plasma source, 6 – Laser-power meter, 7 – ICCD camera synchronized with the laser, 8 – Laser beam, 9 – Fresnel rhomb tandem to turn polarization (if necessary). Reprinted from [14] ©IOP publishing. Reproduced with permission. All rights reserved.

extensions achieve spectrally narrower output, which is often advantageous for LIF experiments. Consequently, LIF using OPO lasers is in minority, though some achievements have been reported [21–23]. Another alternative may be a use of tunable excimer lasers, but this is limited to species that absorb in their relatively narrow tuning range [24]. Also, fluorescence measurements using tunable diode lasers (TDLs) should be mentioned. This technique offers the lowest spectral width of the output line among the mentioned methods, but as the tuning range is strongly limited, it is often insufficient to cover a satisfying number of rotational lines in the molecular spectra. Notable work on atomic LIF by TDL is, for example, [25].

The polarization of the laser output depends on the particular settings of the frequency conversion unit and it should be always cared for. The laser-induced fluorescence can be anisotropic [26]. Also, in most laboratory plasmas, the main scattering mechanism is Rayleigh scattering on the gas particles, causing possibly unwanted background signal. This mechanism does not take place in the direction of the light polarization and can thus be avoided by using horizontally polarized light for excitation. The laser polarization can be turned by 90° using a Fresnel rhomb tandem. A single Fresnel rhomb acts like a quarter wave plate, whereas a tandem of two Fresnel rhombs has an effect similar to half-wave plate, but working for broad-band radiation.

For fluorescence detection, any suitable light detector that can be synchronized with the laser pulses can be used. Photomultiplier tubes give directly temporally resolved result and are very sensitive for low-light detection, but using them for spatially resolved results is a difficult and

often lengthy task. Nevertheless, notable results have been achieved by point-like measurements, scanning the area of interest [21, 27]. An intensified charge-coupled device (ICCD) camera offers an alternative, which gives directly two-dimensionally resolved results, basically a digital photograph, where the resolution is given mainly by the imaging optics. The modern ICCDs offer short exposure times, down to fractions of a nanosecond. The temporal development of fluorescence can then be obtained by taking a series of fluorescence images with varying delays of the exposure gate with respect to the laser pulse. When both spatial and temporal resolutions are desirable, the criterion for decision could be the amount of points necessary in time versus space.

The laser-induced fluorescence is often not the only light signal. If the investigated medium is an active discharge, it often radiates itself. If this background radiation is stable enough, it can be easily subtracted from the measured signal. Furthermore, the laser light is scattered on the particles of the investigated medium, either by Rayleigh scattering on atoms and molecules or by Mie scattering on larger particles like dust or droplets. The former may be eliminated or suppressed by using horizontally polarized light (see earlier text), but in general, the propagation of scattered laser light in the direction of the detector cannot be totally avoided. The laser and the fluorescence light can be separated either spectrally or temporally, depending on the particular experiment. If the fluorescence lifetime is long enough, the detection gate can be started after the end of the laser pulse, excluding the scattered laser light. Eq. (4), however, calculates the total fluorescence, including the photon emitted during the laser pulse. A correction for the fluorescence that was not acquired this way must be calculated. This is relatively easy, as the temporal development of the fluorescence is given by convolution of the laser pulse with a decay exponential, where the laser pulse temporal shape, the fluorescence lifetime, and the delay of the fluorescence detection gate are necessary inputs.

Another common strategy is the spectral separation. To achieve this, the laser wavelength must sufficiently differ from the wavelength of the fluorescence, often leading to more complicated excitation schemata, like the one in **Figure 3**. The most convenient way is a use of bandpass or edge filters in front of the detector. These usually still transmit a non-negligible amount of scattered laser light, which should be quantified by measuring with laser detuned from the absorption wavelength and then subtracted from the measured fluorescence signal. Some groups have used a grating monochromator instead [27]. This increases the complexity of the setup and decreases the sensitivity of fluorescence detection, with the possible benefit of obtaining spectrally resolved fluorescence. This is important for fundamental fluorescence research, but redundant for routine measurement of concentration.

4.1. The instruments used in our work

- Frequency-doubled pulsed Nd:YAG laser (Quanta-Ray PRO-270-30)
- Dye laser (Sirah-D-24-EG) with either a mixture of Rhodamine B + Rhodamine 101 for 612-nm radiation or Rhodamine 6G for 564 nm. In both cases is the output of the dye laser frequency doubled to achieve the wavelength of OH absorption.
- ICCD camera (PI-MAX 1024RB-25-FG43, 16-bit gray-scale resolution) with a UV-transmitting objective lens.

5. Intensity of the measured fluorescence signal: parasitic effects

When investigating discharges via LIF, the excitation of chosen species usually is not the only consequence of the powerful laser radiation. In the following paragraphs, we would like to highlight the other parasitic effects of the laser-discharge interactions, which can affect the intensity of signal measured by the detector, namely:

- Scattering of laser on the surfaces of the discharge reactor
- Laser-induced fluorescence of used materials
- Laser-induced breakdown or other influences of the discharge
- Photodissociation of reactive species

The importance of laser-surface interactions varies greatly in different types of discharges. Special care should be taken in the case of surface discharges, where the laser beam passes the discharge in the proximity of the surface of electrodes or dielectrics. To avoid these phenomena, several tips can be realized. Where it is possible, the laser-surface interaction can be reduced by the proper choice of materials and discharge design. A smooth surface reduces laser scattering toward detector and the use of materials with low absorption in the OH-excitation wavelength range reduces parasitic fluorescence signals. In order to reduce contact of laser beam with solid surfaces, proper alignment of the beam is advisable, including the use of diaphragms and elimination of reflections to the discharge zone, for example, by means of windows tilted at Brewster angle.

Laser-induced breakdown was observed in dielectric barrier discharges (DBD) [28, 29]. When the laser beam hits the surface of dielectrics, it can cause a release of the electron charges trapped at the dielectrics. That can lead to ignition of the discharge at voltage lower than the regular ignition voltage threshold. It means that the laser pulse can behave as the trigger of the discharge. Moreover, during the measurement the laser can increase the intensity of the discharge and also the intensity of spontaneous emission of OH radicals. To avoid the laser-induced breakdown of AC discharges, it is helpful to synchronize the laser with the discharge and to perform the measurement in such a moment in the period of the supplied voltage when the electric field is not strong enough to allow the breakdown.

Fortunately, most of the parasitic effects are not strongly dependent on the laser wavelength. To determine their influence, we can measure the signal with laser wavelength slightly detuned from the OH absorption line. Then, the detector should register the same amount of the scattered laser, fluorescence of surfaces, and increase of signal caused by artificial breakdown. This signal can be subtracted from the OH fluorescence measurement.

In **Figure 6**, we present the example of strong parasitic effects in the case of measurement of OH radicals in diffuse coplanar dielectric barrier discharge, described in detail in [29]. The fluorescence signal was measured in different phases of the period of the supplied voltage. The dotted line shows the spontaneous emission of discharge measured with laser off, showing that the active discharge occurs mainly in the phase regions of 150–200° and 330–380°. The dash-dotted line is the signal measured with the laser wavelength tuned to the center of the

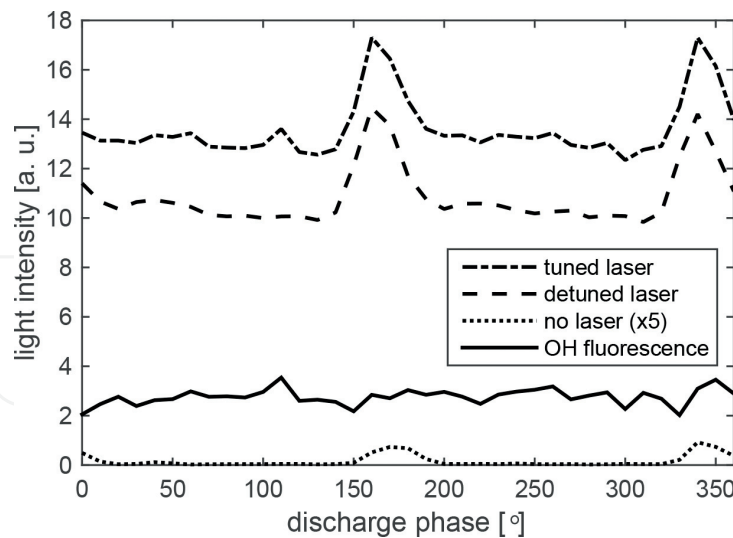


Figure 6. Signal strength vs. discharge phase. Dotted line was measured without laser radiation and is magnified 5 \times . Dash-dotted line is with the laser tuned to the OH absorption line, dashed line is with laser detuned. The solid line is the difference between the dash-dotted and the dashed.

absorption OH line. From that signal it may seem that the concentration of OH radicals is strongly increased during the active discharge. However, very similar evolution can be seen in the dashed line, which represents the measurement performed with laser wavelength detuned from OH absorption line. Since this signal does not include fluorescence of OH radicals induced directly by the laser, its temporary increase must be caused by the artificial breakdown of the discharge. Apart from this temporary increase the dashed line is permanently raised due to the scattered laser radiation and the fluorescence of the dielectric surface. The OH concentration should be calculated from the solid line, i.e. from the difference between the tuned and detuned measurement. Similar problematics of parasitic effects was studied also in [30] for two-photon absorption LIF of atomic hydrogen in a surface DBD.

Another effect which can cause artificial increase of measured signal is photodissociation. The laser photons needed for OH LIF measurement have energy sufficient for dissociation of, for example, ozone molecule. Oxygen atoms then can react with water vapor to form new OH radicals [31]. To cause fluorescence radiation, these artificially created radicals need one photon to be formed and second photon to be excited. Therefore, the photodissociation results in a quadratic increase in the dependence of the signal intensity on the energy of laser pulses. To avoid the effects of photodissociation, the shape of these dependences should be checked and the measurement should be taken in the region of energy where the dependence is not quicker than linear.

6. Intensity of the measured fluorescence signal: saturation effects

Another factor leading to deviation from linear relation of measured fluorescence signal and the exciting laser power is the effect of saturation. It appears with higher laser power when the depletion of the ground state by laser excitation, and the laser-stimulated emission processes are no longer negligible. Under such conditions, further increase of exciting laser power causes lower

increase of fluorescence signal than expected. In the limit of very high laser power, the signal should be no longer dependent on the exciting laser power, leading to theoretically easier evaluation of the measurements [32]. However, in practice it is found that this approach is strongly influenced by spatial and temporal inhomogeneities in the laser beam—in other words, it is quite difficult to guarantee the full saturation conditions across the whole laser beam. This approach is nowadays not very popular and a vast majority of LIF publications works with linear regime. Remaining in the limits of linear regime may be disadvantageous for some experiments due to low fluorescence intensity. Working in partially saturated regime is a possible solution. The partial saturation for 0 – 0 excitation schema was thoroughly investigated in [29]. Let us summarize the main practical results.

Under the condition that rotational energy transfer (RET) in both electronic states is much faster than the spontaneous and collisional deexcitation of the laser-excited electronic state, the dependence of the time-integrated fluorescence intensity M_f on the exciting laser pulse energy E_L can be expressed as

$$M_f(E_f) = \alpha \left(E_f - \frac{p_1 E_f^2}{p_1 E_f + p_2} \left[\frac{e^{-(p_1 E_f + p_2)} - 1}{p_1 E_f + p_2} + 1 \right] \right), \quad (6)$$

where

$$\alpha = N_{Xi} \frac{\kappa B}{c} \tau_0 \left[\sum_{J''\alpha''} F(\lambda_{v''=0J''\alpha''}^{v'=0J'\alpha'}) d(\lambda_{v''=0J''\alpha''}^{v'=0J'\alpha'}) A_{v''=0J''\alpha''}^{v'=0J'\alpha'} f_{v'=0J'\alpha'}(T) \right] \iiint_V D_a \frac{\Omega}{4\pi} s dV \quad (7)$$

describes the theoretical slope that would be observed in the linear case, compare with Eq. (4), and is called *fluorescence gain*. p_1 and p_2 are the parameters describing the saturation. In this form, the equation may be fitted to the measured dependence $M_f(E_f)$ by minimizing the sum of squared residuals with α , p_1 , and p_2 as fit parameters. This formula was found to describe the dependence in the whole range from linear to fully saturated regime quite accurately, but was not practical for use with real-life data. The complexity of the problem caused the fits often to fail and the least-squares optimization was very slow. For this reason, the formula was substituted by a simpler one

$$M_f(E_L) = \frac{\alpha E_f}{1 + \beta E_f}, \quad (8)$$

where β is a parameter describing the degree of saturation, but has no direct physical meaning, as this formula is only an approximative one. The use of formula (8) can be justified by the fact that the second-order polynomial expansion matches with the second-order polynomial expansion of formula (6), and it has been shown that the results are within 10% deviation from the correct value of fluorescence gain α (from fitting Eq. (6)), if the following procedure is followed [29]:

1. First fit the whole range of measured data with the simplified Eq. (8), or its linearized form

$$\frac{1}{M_f(E_f)} = \frac{1}{\alpha E_f} + \frac{\beta}{\alpha}. \quad (9)$$

as the linear fits are very fast and robust. Take the resulting parameter estimates $\hat{\alpha}_0$ and $\hat{\beta}_0$.

2. Check the degree of saturation for the whole energy range. Exclude points with $\hat{\beta}_0 E_f > 1$, reducing the data range such that the simplification (8, 9) can be used. Obviously, if you have no data left after this step, you should adjust the range of laser pulse energies during your next measurement accordingly.

3. Repeat the fit from step 1 with the reduced range. The resulting estimate $\hat{\alpha}_1$ from this fit is now influenced by systematic error due to the use of the simplified equation by less than 10%.

The article [29] deals specifically with 0 – 0 excitation. This was motivated by the fact that the saturation effects were much stronger under conditions with low quenching and long lifetime of the laser-induced fluorescence, where this excitation scheme is advantageously used. For conditions with fast quenching, where the more complicated 0 – 1 → 1 – 1 + 0 – 0 scheme must be used, the saturation effects were usually weak.

7. Collisional processes

The role of collisional processes on quenching and redistribution of excited states was outlined in Section 3. At atmospheric pressure, collisional processes often present the fastest depopulation mechanism of excited states and they need to be taken into account during processing of measured data.

Collisional quenching of excited OH radicals depends on both the vibronic state of OH radical and the type of colliding species. Whereas in rare gases collisional quenching can be negligible when compared with radiative deexcitation (the radiative lifetime of OH(A) is around 700 ns), air at atmospheric pressure reduces the lifetime of excited OH radicals to nanoseconds or fractions of nanoseconds. Water vapor quenches excited OH even by an order of magnitude faster. Strong dependence of excited OH lifetime on the type of collisional partners enables to determine the gas composition, which will be shown in Section 10. On the other hand, this dependence complicates LIF evaluation, especially in environments with inhomogeneous gas composition or temperature.

Second collisional process is the vibrational energy transfer. Since VET noticeably affects the fluorescence spectra, it is important to take into account during LIF data processing especially if the detection sensitivity varies with wavelength. The influence of collisional partners on fluorescence spectra can be demonstrated by comparison of spectra measured in air and in water vapor when OH radicals were excited to the $v' = 1$ state: in air, most of excited OH radicals were transferred to the $v' = 0$ state prior to photon emission and the 0 – 0 band with head located at 306 nm dominated to the fluorescence spectrum. By contrast, the OH(A) lifetime in water vapor was so short that the OH radicals did not have time for VET; most of photons were emitted directly from the $v' = 1$ state and mainly radiation of the 1 – 1 band around 315 nm was observed [33].

When excitation to the $v' = 1$ state is realized, the two fluorescence bands 1 – 1 and 0 – 0 are usually detected. The 0 – 0 vibrational band that results from VET is delayed behind the 1 – 1

band that is activated directly by laser excitation. Similarly, as the temporal evolution of the 1 – 1 band intensity can be described by convolution of the excitation rate (i.e., the temporal profile of laser pulse) with the exponential decay of the $v' = 1$ state, the temporal evolution of the delayed 0 – 0 band can be calculated as a convolution of the temporal profile of the 1 – 1 band (which follows the $v' = 1$ state population) with the exponential decay of the $v' = 0$ state. This holds only when the VET rate constant does not vary during the fluorescence process, that is, when eventual changes of rotational distribution on the $v' = 1$ state do not influence the VET rate strongly.

Third collisional process is the rotational energy transfer, which tends to populate all rotational levels of vibrational states that appear in the fluorescence process. At atmospheric pressure, RET is sometimes so fast that the excited state is practically all the time in rotational equilibrium [20, 34]. In such a case, each vibrational state can be treated as only one effective level, which simplifies the LIF data processing considerably. When RET is not so fast, it is often sufficient to take out the one directly excited rotational level and to suppose that all other rotational levels are in rotational equilibrium [33, 35]. In general, when RET is not fast enough, rotational levels may not reach equilibrium during the OH* lifetime and each vibrational state may be described by its own rotational temperature. Finally, the rotational distribution can be far from any thermalized state and population of each rotational level should be determined individually.

The collisional rate constants for $A^2\Sigma^+(v' = 0)$ and $(v' = 1)$ OH states can be found, for example, in [36–46] for quenching, in [39, 42–45] for VET, and in [45, 47, 48] for RET.

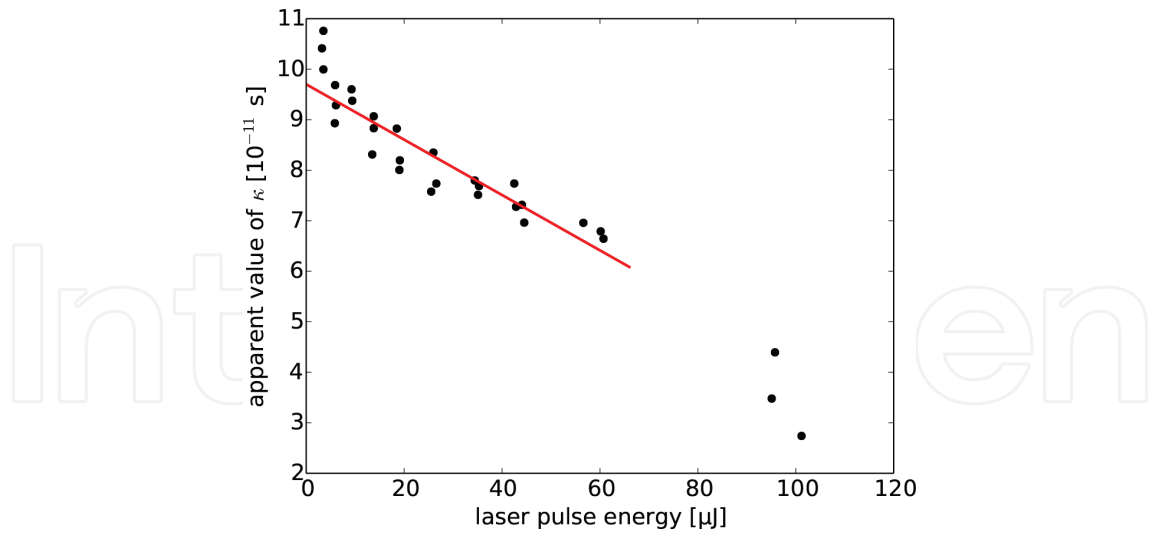
8. Spectral overlap of laser line and absorption line

The measured fluorescence signal depends also on the spectral profile of the laser beam and the absorption line of measured species. That is reflected by the quantity κ appearing in Eqs. (3) and (4)

$$\kappa = \int_{\nu} a(\nu)l(\nu) d\nu, \quad (10)$$

where a is the spectral profile of the absorption line and l spectral profile of the laser, both normalized by $\int_{-\infty}^{\infty} a(\nu)d\nu = \int_{-\infty}^{\infty} l(\nu)d\nu = 1$.

The value of spectral overlap κ can be determined via measurement of the dependence of the fluorescence intensity on the laser wavelength, varied in the vicinity of the absorption line. Resulting spectral profile of measured signal is convolution of the profile of laser line and absorption line. When the laser line profile is known—in our case, the line is assumed to have a Gaussian profile with FWHM 0.4 pm, based on laser specifications from the vendor—the shape of absorption line can be obtained by deconvolution of the laser shape from the measured profile. However, numerical deconvolution is known to be highly sensitive to the noise of experimental data. Alternatively, the absorption line profile can be obtained by least-squares fitting. In that case, the absorption profile can be assumed to have a Voigt shape and the best fit between the convolution of the unknown Voigt profile with the known (or assumed) laser line and the measured profile of the excitation line is found. Then, the value of κ can be calculated using Eq. (10).



dust particles in the gas. When this parasitic signal is eliminated, Eq. (11) enables to determine the value of the unknown integral.

Besides optimization of laser beam shape and discharge apparatus, there are two basic ways on how to eliminate the parasitic signal. The first way can be used when the discharge apparatus can be placed into a vacuum chamber. Since Rayleigh scattering intensity depends on gas pressure whereas scattering on surrounding objects not, it is easy to determine the m_s value from the dependence of measured scattering signal (M_r) on pressure and subtract the parasitic signal from measured data.

However, in some experiments vacuum cannot be used and Rayleigh scattering must be realized in a reactor that is open to ambient atmosphere. Besides laser scattering on reactor parts, dust particles may penetrate to the scattering volume and increase the parasitic signal. In this case, it is possible to use the anisotropy of Rayleigh scattering: Rayleigh scattering does not emit light to the direction parallel with laser polarization. Since scattering on surrounding objects and eventual dust particles does not depend markedly on laser polarization, it is possible to determine the parasitic signal intensity as the signal detected when laser polarization is turned by 90° .

Especially when dust particles can penetrate to the scattering volume, it is desirable to use suitable statistical processing of measured data. If sufficient number of scattering measurements is realized, it is possible to exclude deviating values (e.g., that differ from the mean value by more than triple of sample standard deviation) and/or to calculate the mean value of scattering signals from points between the first and third quartile.

10. Planar LIF in the effluent of a radio-frequency plasma jet

The plasma pencil is a radio-frequency (13.56 MHz)-driven plasma jet ignited in a fused silica capillary (inner diameter 2 mm) with a hollow-driving electrode encompassing the capillary [51, 52]. There is no grounded electrode. The plasma is ignited in argon gas flowing through the capillary and is thus divided from the electrode by a dielectric barrier of the capillary wall. The plasma pencil has been successfully used, for example, for cleaning of historical artifacts [53] or as an excitation source for atomic spectrometry [54]. The power values reported in this section are the power output of the RF generator, not the power absorbed in the plasma.

The argon gas was supplied by a series of pipes. It is known that water molecules adsorbed on the inner walls of pipes are slowly released into the gas phase [55]. The resulting humidity of the working gas is not necessarily unwanted as it allows the formation of OH radicals that play an important role in the plasma jet applications. For serious experiments, however, it should be kept constant and monitored. For this experiment, this was established by humidifying the gas artificially through thin membrane and waiting long enough for the humidity to stabilize. This was verified by measuring the humidity of the feed gas with a capacitive aluminum oxide moisture sensor (Panametrics, MMS 35).

In the effluent of an argon plasma jet, the lifetime of laser-excited OH is longer than the laser pulse and the simpler $0-0$ excitation scheme may be used. To know the rotational temperature of OH(X) that is necessary for the absolute density determination, see Eq. (5), several rotational

absorption lines were probed, namely $R_1(2,4,7)$. Whenever lower rotational temperature was expected (lower driving power or higher argon flow rates), also $R_1(5, 6)$ were probed for accuracy.

To obtain planar-resolved LIF images, the beam expansion optics was used, see **Figure 5**. The thickness of the laser sheet was notably smaller than the inner diameter of the jet capillary; the shown results are thus cross sections through a plane containing the axis of the effluent. The inhomogeneous laser beam profile was determined by acquiring an image of Rayleigh scattering on laboratory air. Prior to this, the detector was tested for the absence of vignetting or other obvious imaging errors. As the laser was propagating horizontally and no significant absorption losses were observed, only the vertical laser profile was of interest: $E(y)$. This is a necessary input for measurement of the fluorescence gain α , see Section 6 about the saturation effects. To obtain the fluorescence gain, a series of fluorescence images were captured, with simultaneously scanning and recording the laser pulse energy. This allows us to form a dependence $M_f(x, y) = f(E_f(y))$ for every pixel of the image and fit Eq. (9) to it. The python code for evaluation could look like this:

```
import numpy
import scipy.stats as st
laser_vertical_profile = numpy.load('laser_profile.npy') #vector
laser_vertical_profile /= numpy.sum(laser_vertical_profile)
#normalize

fluo_vs_pwr = numpy.load('fluo_vs_pwr.npy') #3D array - series of
ICCD images
                #axes: 0-frame no. 1-vertical, 2-horizontal
laser_pulse_Es = numpy.load('laser_pulse_Es.npy') #vector

#usually, fluorescence images are accumulated over several laser
Pulses
#this is to get them on the same scale
#assumption: the laser pulse energy does not change much during
#acquiring a single image
ratio = len(laser_pulse_Es) // len(fluo_vs_pwr) #integer division
laser_Es = numpy.zeros(len(fluo_vs_pwr))
for i in range(len(fluo_vs_pwr)):
    #calculate mean energy of laser pulses measured during the
    #accumulation of each fluorescence image
    laser_Es[i] = numpy.mean(laser_pulse_Es[i*ratio:(i+1)*ratio])

#run fit of every pixel
#z denotes the number of the image zmax,
ymax, xmax = fluo_vs_pwr.shape
alphas = numpy.zeros((ymax, xmax))
alphas_errors = numpy.zeros((ymax, xmax))
for y in range(ymax):
```

```

#prepare the laser-pulse-energy vector for the y-position
en_y = numpy.zeros(zmax)
for frame in range(zmax):
    en_y[frame] = laser_Es[frame] * laser_vertical_profile[y]
for x in range(xmax):
    inv_lif = fluo_vs_pwr[:,y,x]**(-1)
    slope,intercept,r,p,stderr = st.linregress(en_y**(-1), inv_lif)
    alpha0 = 1/slope
    beta0 = intercept*alpha0
    #second-round fit with restricted range
    slope,intercept,r,p,stderr = st.linregress(en_y[(en_y*beta0)<1]**(-1),
                                                inv_lif[(en_y*beta0)<1])

    alpha1 = 1/slope
    beta1 = intercept*alpha1
    #keep the result in 2D array of alphas
    alphas[y,x] = alpha1
    alphas_errors[y,x] = stderr

```

Here, we have advantageously used the linearized Eq. (9) and the `linregress` function of `scipy.stats` library, which calculates the best fitting parameters analytically and is thus fast and robust.

Probing several absorption lines and calculating their fluorescence gain for each pixel allows estimating the rotational temperature with planar resolution, see the example in **Figures 8** and **9** and Eq. (5). Rotational temperature is often expected to agree with the kinetic temperature of the gas. The molecular fluorescence can be thus used for thermometry with very high spatial resolution, disturbing the measured plasma only weakly compared to most other thermometric

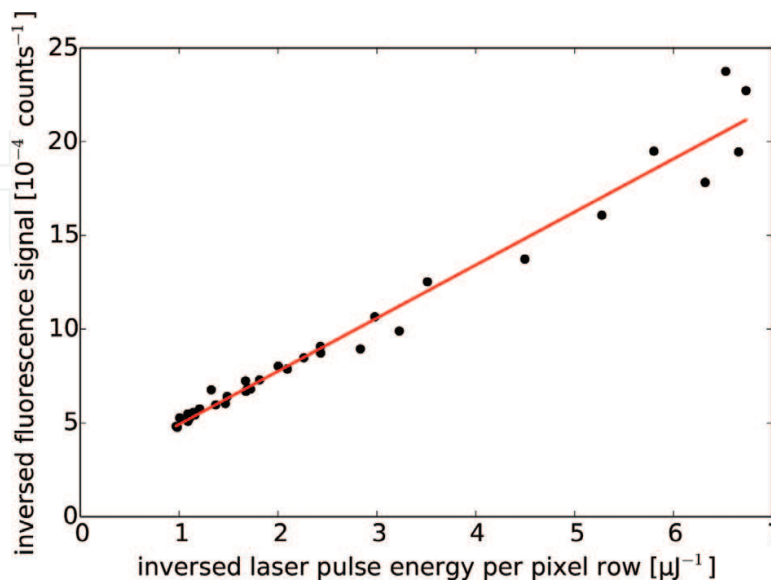


Figure 8. An example of the fluorescence gain determination. In the shown case, the fluorescence gain $\alpha = (3500 \pm 100)$ counts/ μ .

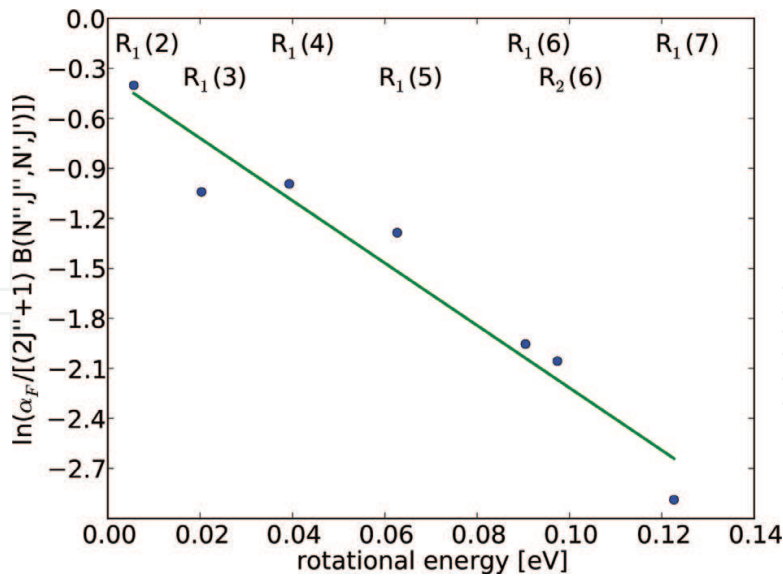


Figure 9. Fluorescence gains obtained from probing different absorption lines show Boltzmann distribution corresponding to rotational temperature $T = (620 \pm 9)$ K. J'' is the quantum number of the probed lower state and B is the absorption coefficient of the transition. Reprinted from [14] ©IOP publishing. Reproduced with permission. All rights reserved.

methods, but with the assumption that the investigated plasma source and the laser profile stay stable for the whole measurement time. An example of such temperature measurement is shown in **Figure 10**. A result of gas dynamics simulation is added for comparison. The simulation considers a simplified case without plasma, where hot argon is blown into room-temperature air. For further details, see [14].

To obtain the absolute concentration, the quantum gain of the fluorescence is also necessary, that is, the fraction of laser-excited molecules that got quenched must be quantified. In practice, the real fluorescence lifetime is measured and compared with the natural lifetime of the laser-excited state. As mentioned in Section 4, the fluorescence lifetime may be measured by taking a series of short-exposure fluorescence images with varying delays after the laser pulse. The gate width was set to 5 ns, which was sufficient for this task, as the OH fluorescence lifetime in argon is expected to be in the order of tens to hundreds of nanoseconds. The fluorescence decay for the 0 – 0 excitation scheme is expected to follow a single exponential, provided that the rotational energy transfer is much faster, which was satisfied in this case. Like the fluorescence gain parameter α , also the fluorescence lifetime τ is space-dependent. To evaluate the series of images and obtain a map of fluorescence lifetimes, a code similar to that for the fluorescence gain α was used. The theoretical function $M_f(t) = Ae^{-t/\tau}$ could in principal be linearized by taking a logarithm, but in practice, a constant offset was found to be non-negligible, so the model function was $M_f(t) = Ae^{-t/\tau} + C$, which cannot be linearized anymore. Nevertheless, the implementation of Levenberg–Marquardt algorithm available in `scipy` or `lmfit` libraries was found to work satisfactorily fast and robust, see an example fit in **Figure 11**.

The map of fluorescence lifetimes is not only necessary for calculating the map of OH concentration but also contains information about the local quenching rate. For simple cases where only two nonreactive gas environments with sufficiently different quenching rates meet, this can be used to estimate the mixing ratio at each position. For the resulting fluorescence lifetime τ holds.

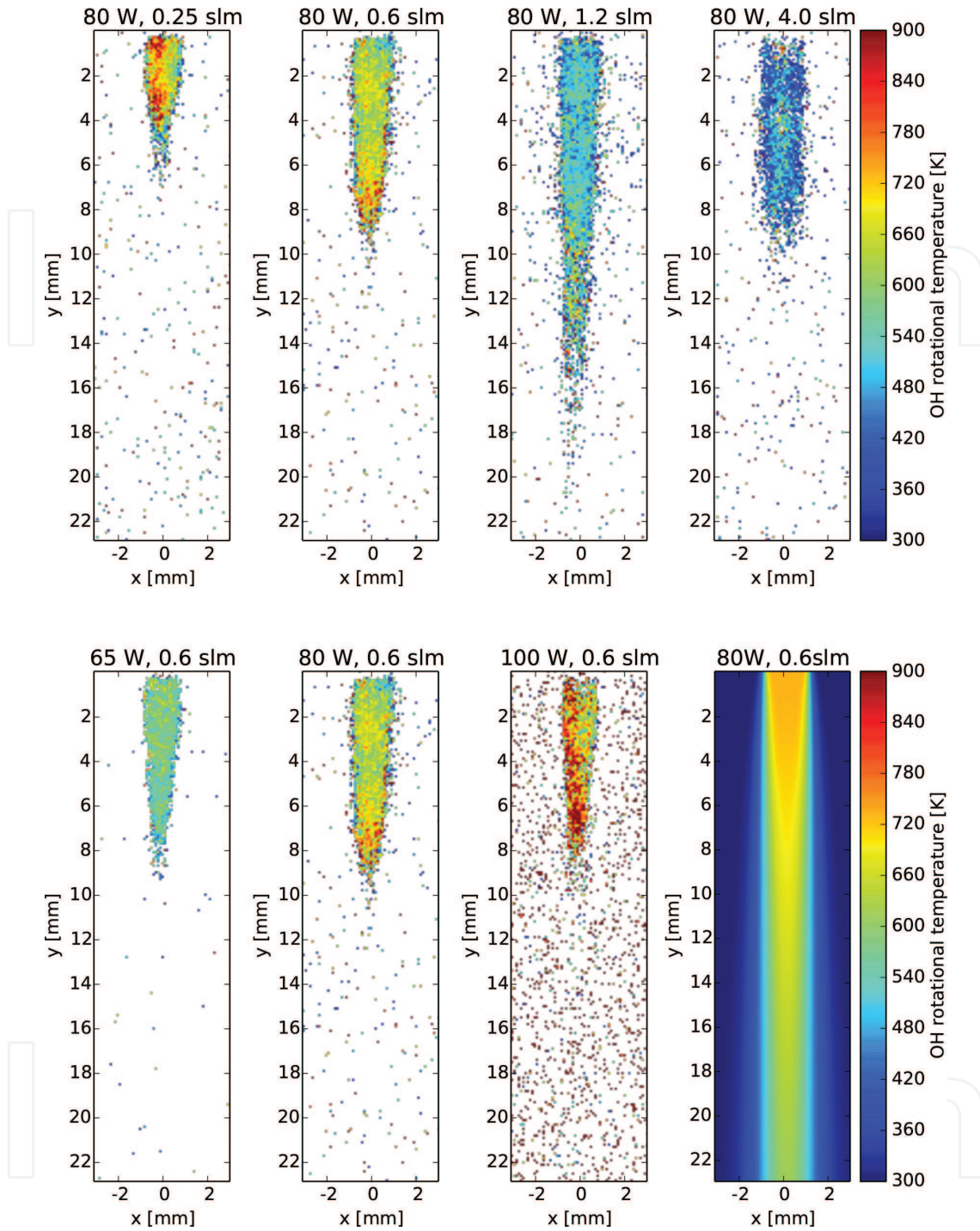


Figure 10. Measured discharge temperature for various discharge conditions. Bottom-right: Result of gas dynamics simulation (no plasma taken into account) for comparison. Reprinted from [14] © IOP publishing. Reproduced with permission. All rights reserved.

$$\frac{1}{\tau} = \sum_{j''\alpha'\alpha''} f_{v'=0j'\alpha'}(T) A_{v''=0j''\alpha''}^{v'=0j'\alpha'} + \sum_i n_i q_i(T) \quad (12)$$

where n_i is the concentration of collision partner i and $q_i(T)$ is its temperature-dependent quenching coefficient in $\text{m}^3 \text{s}^{-1}$. To estimate the argon-air mixing ratio, a set of theoretical

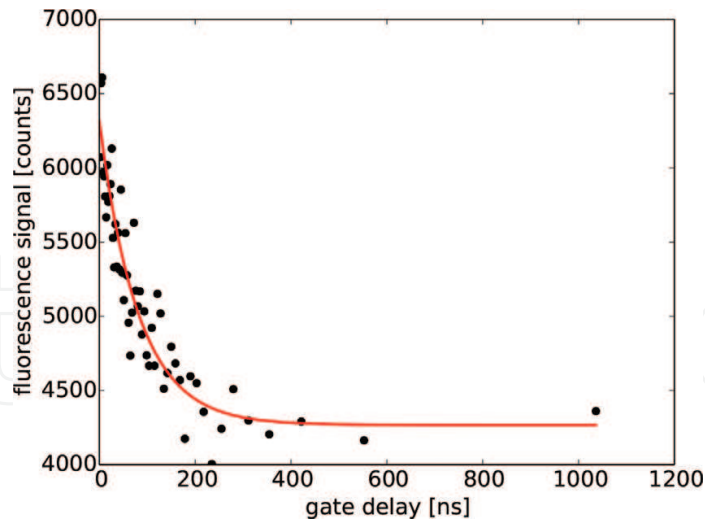


Figure 11. An example of the single exponential fit to the measured decay of the fluorescence signal at one pixel for RF driving power of 80 W and argon flow rate of 0.6 slm. The fitted lifetime is $\tau = (81 \pm 10)$ ns. Reprinted from [14] ©IOP publishing. Reproduced with permission. All rights reserved.

fluorescence developments was simulated with LASKIN [56] for humid air and humid argon for the whole range of temperatures found in the preceding experiments in steps of 25 K. For each condition, a set of unique pairs temperature-lifetime was assembled. The amount of water in air was 1.3 volume percent (found by laboratory hygrometer), the amount of water in argon was dependent on the flow rate and was measured by the precise hygrometer coupled to the argon supply (ranging from 160 to 1030 volume ppm). The mixing ratio was then calculated by

$$\frac{n_{\text{air}}}{n_{\text{air}} + n_{\text{Ar}}} = \frac{1/\tau_{\text{meas}}(x, y) - 1/\tau_{\text{Ar}}(T(x, y))}{1/\tau_{\text{air}}(T(x, y)) - 1/\tau_{\text{Ar}}(T(x, y))} \quad (13)$$

where (x, y) are pixel coordinates, $\tau_{\text{meas}}(x, y)$ is the measured lifetime as a result of the single exponential fit for each pixel, $\tau_{\text{Ar}}(T(x, y))$ and $\tau_{\text{air}}(T(x, y))$ are the theoretical lifetimes from the LASKIN simulations for humid argon and air, respectively. The temperature was taken from the rotational temperature measurement mentioned earlier. The resulting maps of mixing ratio are shown in **Figure 12**. The zone with low air admixture elongates with the increase of argon flow rate up to 2–3 slm, when transition to turbulent flow appears. A similar method was used by Yagi et al. for spatially resolved measurement of humidity based on quenching of NO radical [57]. For further investigations of gas dynamics in plasma jets, see also [58–60].

Finally, in **Figures 13** and **14**, the measured maps of OH concentration are shown with the images of the spontaneous plasma emission for comparison. It can be clearly seen that the regions with the highest OH concentration do not coincide with the regions with the strongest plasma emission. On the contrary, the highest OH concentration was found downstream from the tip of the visible discharge. Furthermore, we observe a hollow profile of OH concentration, which is the most pronounced for the highest argon flow rate of 4.0 slm. These conditions were also those with the lowest humidity of the feed gas, so this hollow profile is attributed to the amount of water molecules available for dissociation by collisions with the active particles of the plasma—mainly electrons and argon metastables.

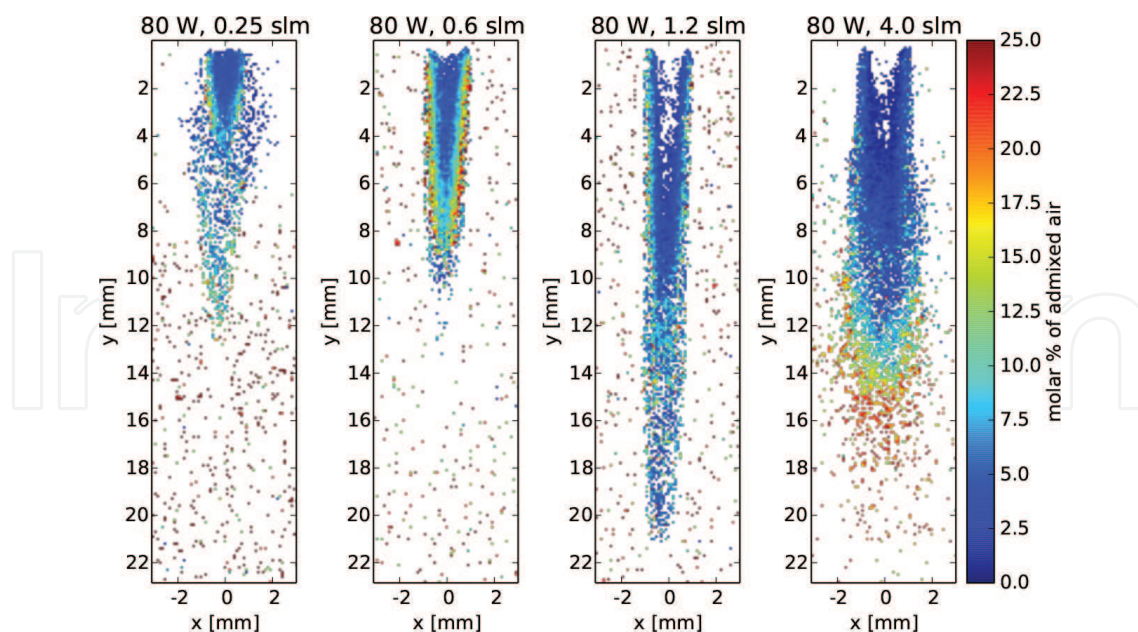


Figure 12. Maps of molar percent of ambient air admixed into the argon effluent of the plasma pencil for various conditions. The points with fluorescence lifetime uncertainty greater than 25% are displayed as white. Reprinted from [14] ©IOP publishing. Reproduced with permission. All rights reserved.

We have seen that the final result—map of OH concentration—consists of many steps, which means that this diagnostic method is not an easy one. On the other hand, proper evaluation of each of these steps has provided a very complex information about the active zone of the plasma jet effluent which can bring deep insight into the processes occurring there.

11. Surface DBD in water vapor

An example of a challenging LIF experiment is the OH measurement in a surface coplanar DBD ignited in water vapor at atmospheric pressure [33]. The coplanar DBD is made of a system of coplanar strip electrodes that are covered by a ceramic and plasma is created in the gas on the opposite side of the ceramic. The neighboring strip electrodes are charged with opposite polarity, which enables to cover a large area of the ceramic by macroscopically homogeneous plasma [61–63]. Since plasma layer is only 0.3-mm thick, the density of the power delivered to the discharge is high and the discharge is expected to generate high concentration of reactive radicals. Certainly, the small thickness complicates fluorescence investigation: all parasitic effects resulting from laser-surface interactions that are discussed in Section 5 can be expected and a good spatial resolution is required.

In order to generate a source of OH radicals that does not produce a number of other reactive species and that could be used for a specific surface treatment, the coplanar DBD was ignited in pure water vapor. In order to prevent water condensation at atmospheric pressure, a heated reactor was built, and both the electrode system and reactor walls were heated to 120°C. Again, water atmosphere complicates fluorescence measurements since water is a very

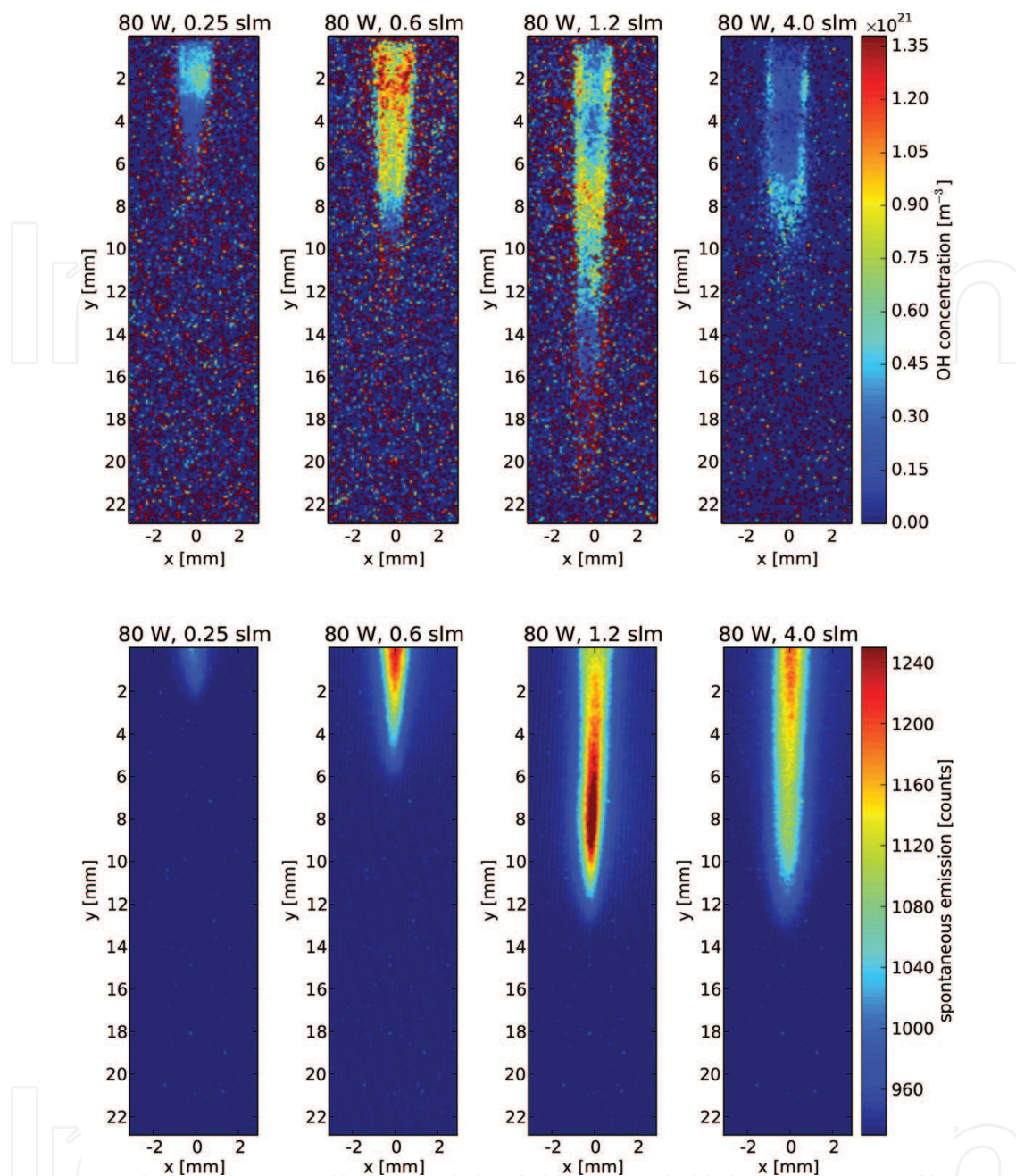


Figure 13. Maps of OH concentration for different argon flow rates (top) with images of spontaneous plasma emission (bottom). Reprinted from [14] ©IOP publishing. Reproduced with permission. All rights reserved.

effective quencher of excited OH radicals, which reduces their lifetime below 100 ps. In order to minimize reflections of laser beam, the windows for laser input and output were tilted at Brewster angle.

Due to the short lifetime of the excited OH state, it was necessary to excite OH radicals to the vibrationally excited state, and emission from both ($v' = 0, 1$) vibronic states was taken into account. The RET was not fast enough to establish rotational equilibrium during the short lifetime, which led to an overpopulation of the directly excited rotational level that had to be treated separately during the processing of measured data.

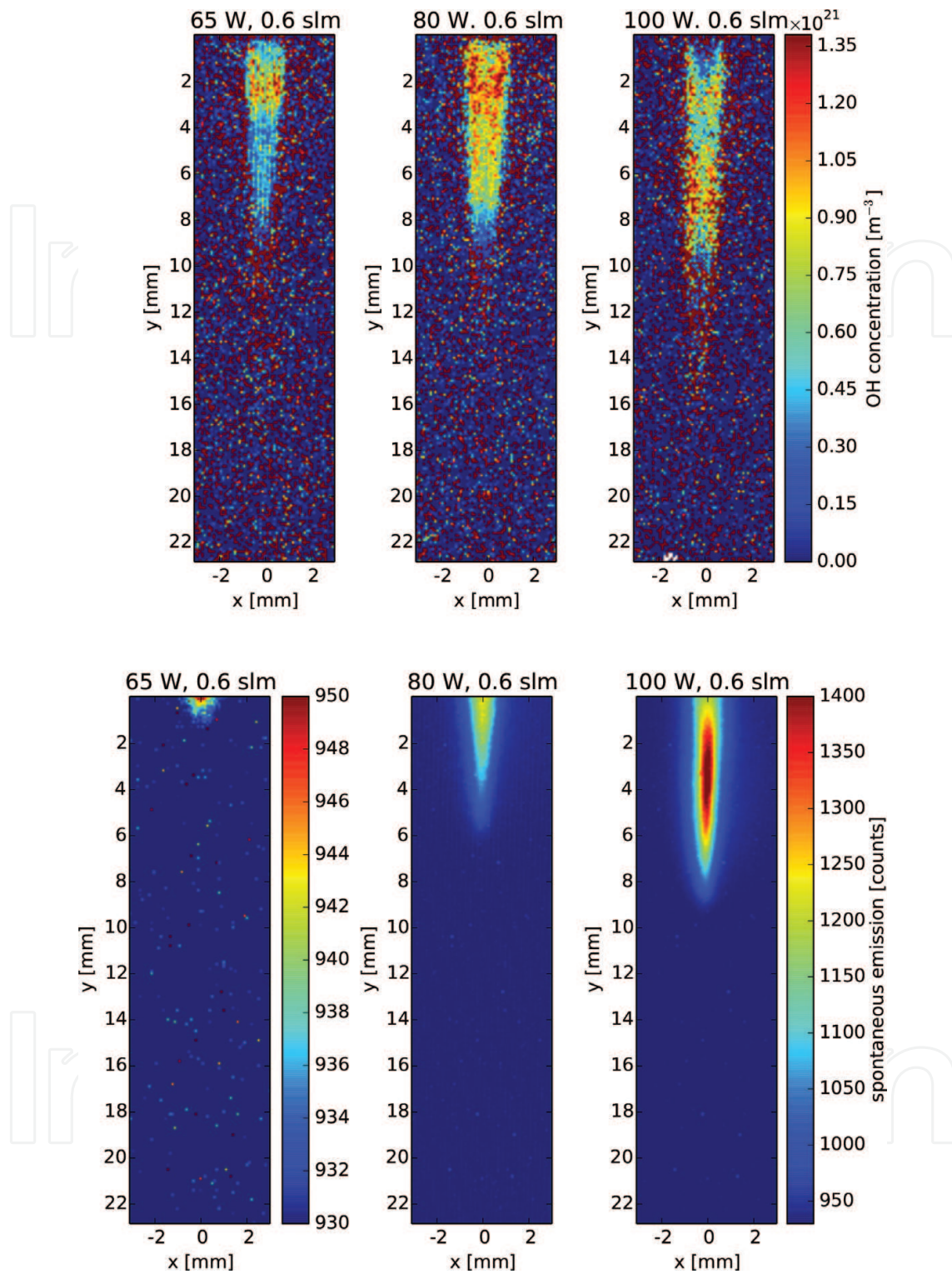


Figure 14. Maps of OH concentration for different values of driving power (top) with images of spontaneous plasma emission (bottom). Reprinted from [14] ©IOP publishing. Reproduced with permission. All rights reserved.

As discussed in Section 5, it was necessary to subtract the parasitic signal of scattered laser radiation and fluorescence of the dielectrics, which both can be quantified by means of the signal that was measured when laser wavelength was detuned from the absorption line of OH radicals. This measurement was further useful for detection of water droplets. Although they

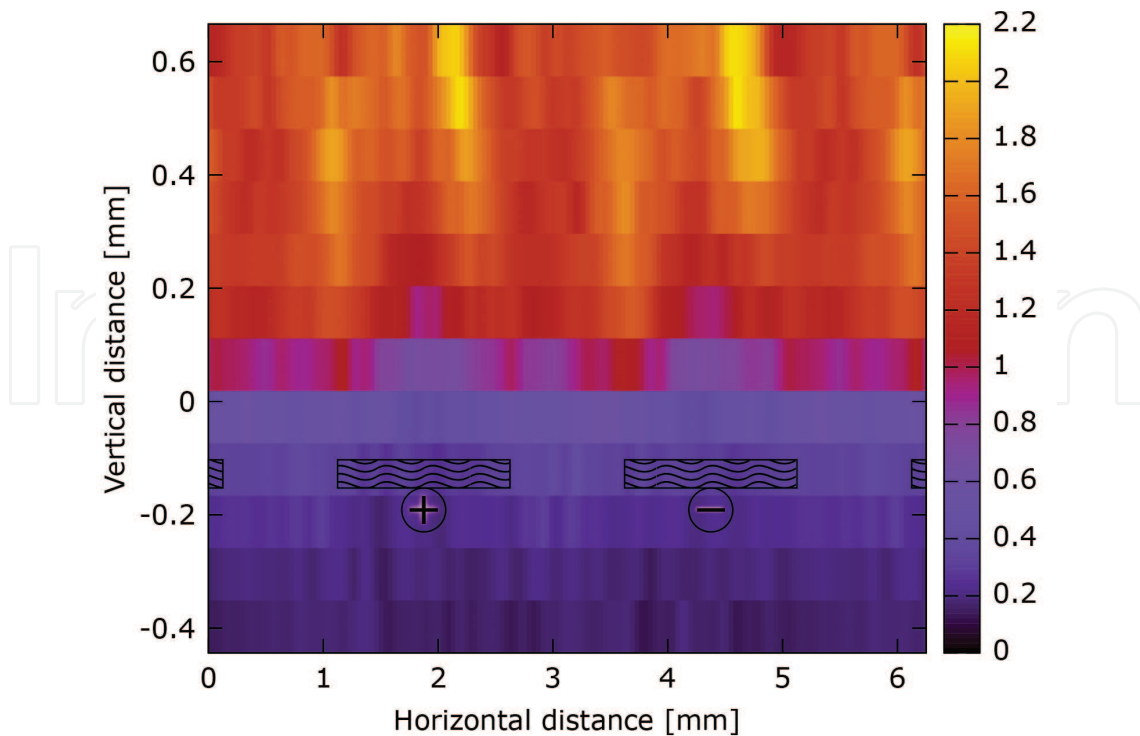


Figure 15. Laser radiation scattered on water droplets that were present in the coplanar DBD ignited in water vapor. Measured with laser wavelength detuned from the absorption line of OH radicals. Reprinted from [33] ©IOP publishing. Reproduced with permission. All rights reserved.

were not visible by naked eye, water droplets were really present in the gas phase as demonstrated in **Figure 15**. In order to eliminate spontaneous discharge emission, detection of droplets was realized in such a part of the period of the supplied voltage, when electric field was weak and it was not possible to ignite a discharge event. The shown distribution of droplets was not uniform—the scattering signal was weak in the discharge region, where gas was heated and droplets evaporated quickly. In addition, we can see an increased signal above electrode edges that demonstrates that besides direct gas heating there is another influence of discharge on the distribution of water droplets.

Another parasitic (from the fluorescence point of view) signal is the spontaneous discharge emission. Also, this signal is useful from another point of view and it enables, for example, to determine the spatial structure of discharge. In order to increase the signal-to-noise ratio in short measurements required for high temporal resolution, it is possible to synchronize the discharge event with the measurement by a laser shot with wavelength detuned from OH absorption line. In such a case, the signal of scattered laser radiation should be subtracted from the measured picture. An example of obtained spatial structure of the coplanar DBD is shown in **Figure 16**. It demonstrates that in water vapor the discharge is located namely above the area between electrodes.

After subtraction of parasitic signals, the LIF data can be finally used for the determination of OH concentration. As shown in **Figure 17**, the distribution of OH radicals followed well the shape of the visible discharge that bridged the interelectrode area. The OH concentration reached the value $5 \times 10^{20} \text{ m}^{-3}$, which was by an order of magnitude higher than OH

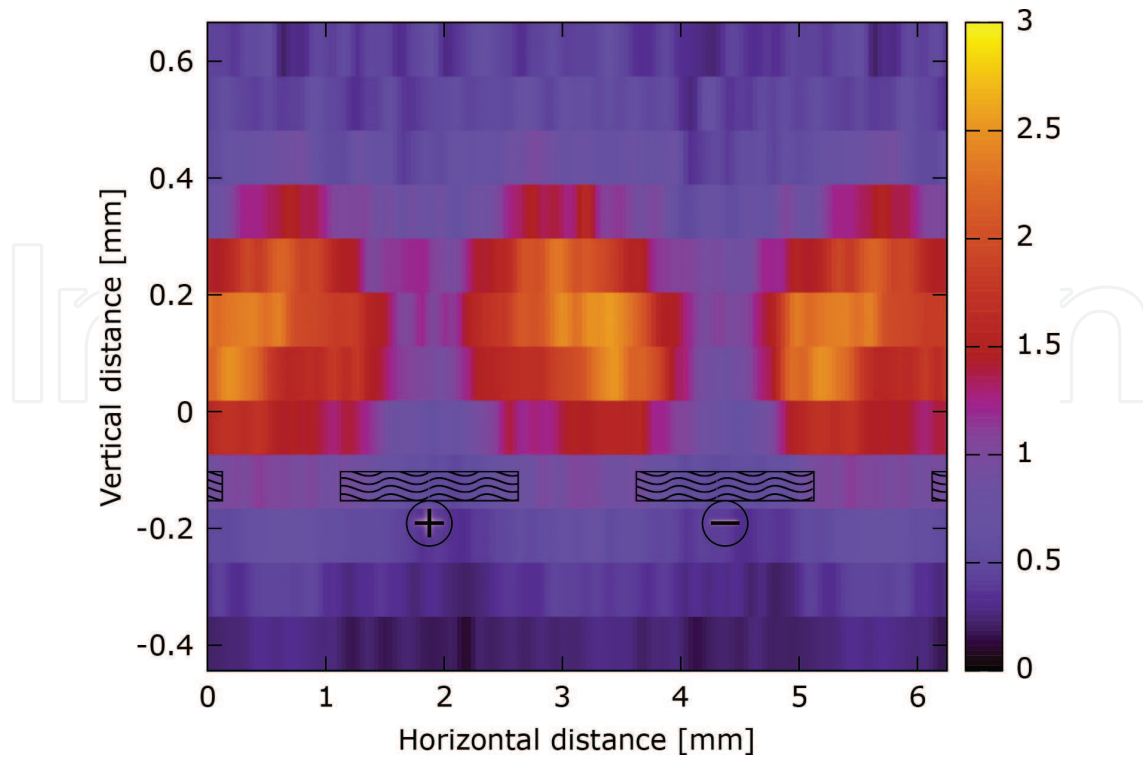


Figure 16. Emission of DBD ignited in water vapor at atmospheric pressure. Discharge ignition was synchronized with ICCD measurement by a laser shot. Reprinted from [33] ©IOP publishing. Reproduced with permission. All rights reserved.

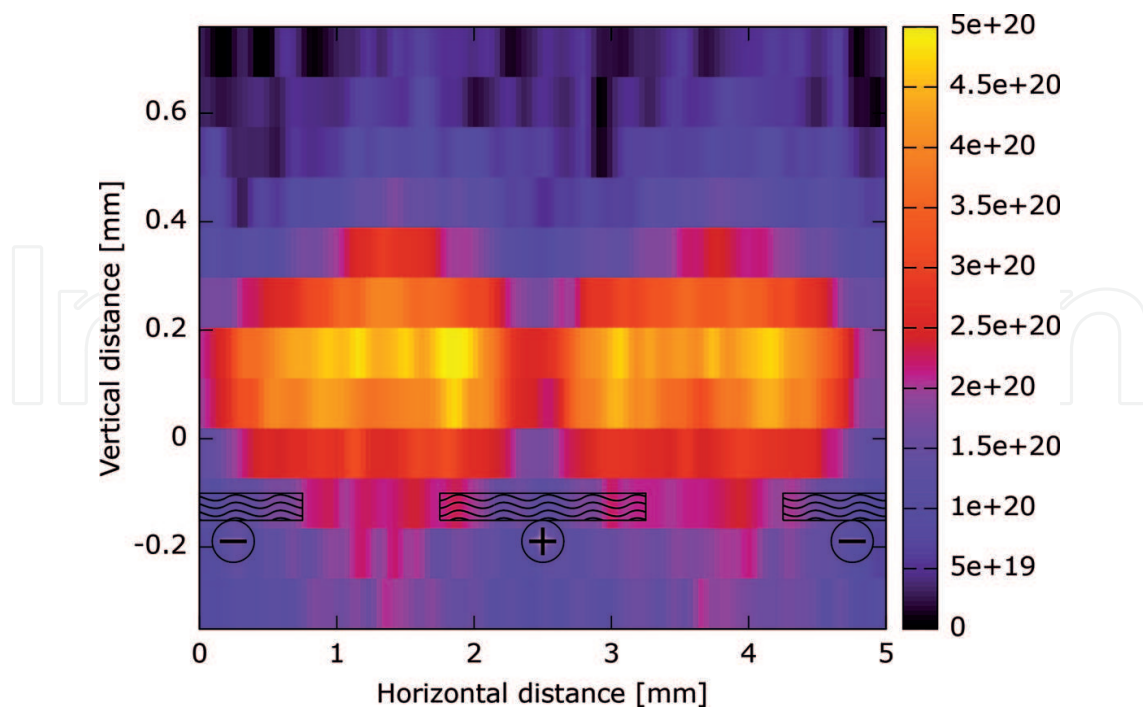


Figure 17. OH concentration determined by fluorescence measurement in the coplanar DBD ignited in water vapor at atmospheric pressure. Reprinted from [33] ©IOP publishing. Reproduced with permission. All rights reserved.

concentration in analogical discharge ignited in air (with relative humidity of 40%). By means of two-photon absorption LIF of atomic hydrogen and by optical emission spectrometry, it was verified that plasma in pure water vapor generated almost solely OH radicals, concentration of other reactive radicals was negligible. As a result, the LIF method proved that the investigated discharge can be used as a selective source of oxidizing OH radicals with relatively high concentration [33].

Acknowledgements

This research has been supported by the project LO1411 (NPU I) funded by the Ministry of Education, Youth and Sports of Czech Republic and by the Czech Science Foundation projects 16-09721Y and 17-04329S.

Author details

Jan Voráč*, Pavel Dvořák and Martina Mrkvičková

*Address all correspondence to: vorac@mail.muni.cz

Department of Physical Electronics, Faculty of Science, Masaryk University, Brno, Czech Republic

References

- [1] Voráč J, Synek P, Procházka V, Hoder T. State-by-state emission spectra fitting for non-equilibrium plasmas: Oh spectra of surface barrier discharge at argon/water interface. *Journal of Physics D: Applied Physics*. 2017;**50**:294002
- [2] Isaksen I, Dalsøren S. Getting a better estimate of an atmospheric radical. *Science*. 2011;**331**(6013):38-39
- [3] Lee JH, Park JW, Lee HB. Cell adhesion and growth on polymer surfaces with hydroxyl groups prepared by water vapour plasma treatment. *Biomaterials*. 1991;**12**(5):443-448
- [4] Sun B, Sato M, Clements J. Use of a pulsed high-voltage discharge for removal of organic compounds in aqueous solution. *Journal of Physics D: Applied Physics*. 1999;**32**(15):1908
- [5] Repine J, Fox RB, Berger E. Hydrogen peroxide kills *Staphylococcus aureus* by reacting with staphylococcal iron to form hydroxyl radical. *Journal of Biological Chemistry*. 1981;**256**(14):7094-7096
- [6] Tiedemann A. Evidence for a primary role of active oxygen species in induction of host cell death during infection of bean leaves with *Botrytis cinerea*. *Physiological and Molecular Plant Pathology*. 1997;**50**(3):151-166

- [7] Visseren FL, Verkerk M, Van Der Bruggen T, Marx J, Van Asbeck B, Diepersloot R. Iron chelation and hydroxyl radical scavenging reduce the inflammatory response of endothelial cells after infection with chlamydia pneumoniae or inuenza a. *European Journal of Clinical Investigation*. 2002;**32**(s1):84-90
- [8] Dieke G, Crosswhite H. The ultraviolet bands of oh fundamental data. *Journal of Quantitative Spectroscopy and Radiative Transfer*. 1962;**2**(2):97-199
- [9] Luque J, Crosley DR. Transition probabilities in the $A^2\Sigma^+-X^2\Pi$ electronic system of OH. *The Journal of Chemical Physics*. 1998;**109**(2):439-448
- [10] Luque J, Crosley D. Lifbase: Database and spectral simulation program (version 1.5). SRI international report MP. 1999;**99**(009)
- [11] Herzberg G, Spinks JWT. *Molecular Spectra and Molecular Structure: Diatomic molecules*. Van Nostrand: Princeton, 1950
- [12] Lefebvre-Brion H, Field RW. *The Spectra and Dynamics of Diatomic Molecules*. Elsevier Academic Press. 2004
- [13] Luque J, Crosley D. Lifbase: Database and spectral simulation program (version 1.5), vol. 99, 1999
- [14] Voráč J, Obrusník A, Procházka V, Dvořák P, Talába M. Spatially resolved measurement of hydroxyl radical (OH) concentration in an argon RF plasma jet by planar laser-induced fluorescence. *Plasma Sources Science and Technology*. 2014;**23**:025011
- [15] Verreycken T, Mensink R, van der Horst R, Sadeghi N, Bruggeman PJ. Absolute OH density measurements in the effluent of a cold atmospheric-pressure Ar-H₂O RF plasma jet in air. *Plasma Sources Science Technology*. 2013;**22**:055014
- [16] Li L, Nikiforov A, Xiong Q, Britun N, Snyders R, Lu X, Leys C. OH radicals distribution in an Ar-H₂O atmospheric plasma jet. *Physics of Plasmas*. 2013;**20**:093502
- [17] Lu X, Naidis GV, Laroussi M, Reuter S, Graves DB, Ostrikov K. Reactive species in non-equilibrium atmospheric-pressure plasmas: Generation, transport, and biological effects. *Physics Reports*. 2016;**630**:1
- [18] Yonemori S, Ono R. Flux of OH and O radicals onto a surface by an atmospheric-pressure helium plasma jet measured by laser-induced fluorescence. *Journal of Physics D: Applied Physics*. 2014;**47**:125401
- [19] K. Kohse-Höinghaus. Laser techniques for the quantitative detection of reactive intermediates in combustion systems. *Progress in Energy and Combustion Science*. 1994;**20**(3): 203-279
- [20] Voráč J, Dvořák P, Procházka V, Ehlbeck J, Reuter S. Measurement of hydroxyl radical (OH) concentration in an argon RF plasma jet by laser-induced fluorescence. *Plasma Sources Science and Technology*. 2013;**22**(2):025016
- [21] Yonemori S, Nakagawa Y, Ono R, Oda T. Measurement of oh density and air-helium mixture ratio in an atmospheric-pressure helium plasma jet. *Journal of Physics D: Applied Physics*. 2012;**45**(22):225202

- [22] Lee Y-H, Maus RG, Smith BW, Winefordner JD. Laser-induced fluorescence detection of a single molecule in a capillary. *Analytical Chemistry*. 1994;**66**(23):4142-4149
- [23] Giamarchi P, Burel L, Stephan L, Lijour Y, Le Bihan A. Laser-induced fluorescence with an opo system. Part i. optimisation of the analytical system by use of experimental design methodology. application to the direct quantification of traces of benzo [a] pyrene. *Analytical and Bioanalytical Chemistry*. 2002;**374**(3):490-497
- [24] Andresen P, Bath A, Gröger W, Lülff H, Meijer G, Ter Meulen J. Laser-induced fluorescence with tunable excimer lasers as a possible method for instantaneous temperature field measurements at high pressures: checks with an atmospheric ame. *Applied Optics*. 1988;**27**(2):365-378
- [25] Vitelaru C, Aniculaesei C, De Poucques L, Minea T, Boisse-Laporte C, Bretagne J, Popa G. Tunable diode-laser induced fluorescence on al and ti atoms in low pressure magnetron discharges. *Journal of Physics D: Applied Physics*. 2010;**43**(12):124013
- [26] Brockhinke A, Kreutner W, Rahmann U, Kohse-Höinghaus K, Settersten TB, Linne MA. Timewavelength-and polarization-resolved measurements of OH($A^2\Sigma^+$) picosecond laser-induced fluorescence in atmospheric-pressure flames. *Applied Physics B: Lasers and Optics*. 1999;**69**(5):477-485
- [27] Riès D, Dilecce G, Robert E, Ambrico P, Dozias S, Pouvesle JM. LIF and fast imaging plasma jet characterization relevant for NTP biomedical applications. *Journal of Physics D: Applied Physics*. 2014;**47**(27):275401
- [28] Ambrico P, Ambrico M, Šimek M, Colaianni A, Dilecce G, De Benedictis S. Laser triggered single streamer in a pin-to-pin coplanar dielectric barrier discharge. *Applied Physics Letters*. 2009;**94**(23):231501
- [29] Voráč J, Dvořák P, Procházka V, Morávek T, Ráhel J. Dependence of laser-induced fluorescence on exciting-laser power: Partial saturation and laser-plasma interaction. *The European Physical Journal Applied Physics*. 2015;**71**(2):20812
- [30] Mrkvičková M, Ráhel J, Dvořák P, Trunec D, Morávek T. *Plasma Sources Science and Technology*. 2016;**25**:055015
- [31] Teramoto Y, Kim H-H, Ogata A, Negishi N. Measurement of OH ($X^2\Sigma$) in immediate vicinity of dielectric surface under pulsed dielectric barrier discharge at atmospheric pressure using two geometries of laser-induced fluorescence. *Journal of Applied Physics*. 2014;**115**:133302
- [32] Piepmeier E. Theory of laser saturated atomic resonance fluorescence. *Spectrochimica Acta B: Atomic Spectroscopy*. 1972;**27**(10):431-443
- [33] V. Procházka, Tučeková Z, Dvořák P, Kováčik D, Slavíček P, Zàhoranová A, Voráč J. Coplanar surface barrier discharge ignited in water vapour - a selective source of OH radicals proven by (TA)LIF measurement. *Plasma Sources Science and Technology*. 2017;**27**:015001

- [34] Vorac J, Prochazka V, Dvorak P. Vibrational and rotational energy transfer in a (2) sigma (+) state of oh radicals measured by laser induced fluorescence. *CHEMICKE LISTY*. 2012;**106**: S1504-S1507
- [35] Dunn M, Masri A. A comprehensive model for the quantification of linear and nonlinear regime laser-induced fluorescence of oh under a²σ+ x²π (1, 0) excitation. *Applied Physics B*. 2010;**101**(1-2):445-463
- [36] Dilecce G, Ambrico PF, Simek M, Benedictis SD. LIF diagnostics of hydroxyl radical in atmospheric pressure He-H₂O dielectric barrier discharges. *Chemical Physics*. 2012;**398**: 142-147
- [37] Copeland RA, Crosley DR. Rotational level dependence of electronic quenching of OH (A ²Σ⁺, v' = 0). *Chemical Physics Letters*. 1984;**7**(3):295-300
- [38] Copeland RA, Dyer MJ, Crosley DR. Rotational level dependence of electronic quenching of OH(A ²Σ⁺, v' = 0). *Journal of Chemical Physics*. 1985;**82**:4022-4032
- [39] Copeland RA, Wise ML, Crosley DR. Vibrational energy transfer and quenching of hydroxyl (A ²Σ⁺, v' = 1). *Journal of Chemical Physics*. 1988;**92**:5710
- [40] Wysong IJ, Jeffries JB, Crosley DR. Quenching of A ²Σ⁺ OH at 300K by several colliders. *Journal of Chemical Physics*. 1990;**92**:5218-5222
- [41] Bailey AE, Heard DE, Henderson DA, Paul PH. Collisional quenching of OH(A ²Σ⁺, v' = 0) by H₂O between 211 and 294K and the development of a unified model for quenching. *Chemical Physics Letter*. 1999;**302**:132-138
- [42] Williams LR, Crosley DR. Collisional vibrational energy transfer of OH(A ²Σ⁺, v' = 1). *Journal of Chemical Physics*. 1996;**104**:6507
- [43] Hartlieb AT, Markus D, Kreutner W, Kohse-Hoeinghaus K. Measurement of vibrational energy transfer of OH(A ²Σ⁺, v' = 1→0) in low pressure. *Applied Physics B*. 1997;**65**:81-91
- [44] Rahmann U, Kreutner W, Kohse-Hoeinghaus K. Rate-equation modeling of single and multiple quantum vibrational energy transfer of OH(A ²Σ⁺, v' = 0 to 3). *Applied Physics B*. 1999;**69**(1):61-70
- [45] J. Burris, J. Butler, T. McGee, and W. Heaps, Collisional deactivation rates for (A ²Σ⁺, v' = 1) state of OH. *Chemical Physics*. 1988;**124**(2):251-258
- [46] Burris J, Butler J, McGee T, Heaps W. Quenching and rotational transfer rates in the v' = 0 manifold of OH(A ²Σ⁺). *Chemical Physics*. 1991;**151**:233-238
- [47] Joerg A, Meier U, Kienle R, Kohse-Hoeinghaus K. State-specific rotational energy transfer in OH(A ²Σ⁺; v' = 0) by some combustion-relevant collision partners. *Applied Physics B*. 1992;**55**:305
- [48] Kienle R, Joerg A, Kohse-Hoeinghaus K. State-to-state rotational energy transfer in OH (A ²Σ⁺; v' = 1). *Applied Physics B*. 1993;**56**:249-258
- [49] Miles RB, Lempert WR, Forkey JN. Laser rayleigh scattering. *Measurement Science and Technology*. 2001;**12**(5):R33

- [50] Bucholtz A. Rayleigh-scattering calculations for the terrestrial atmosphere. *Applied Optics*. 1995;**34**(15):2765-2773
- [51] Janca J, Klima M, Slavicek P, Zajickova L. HF plasma pencil-new source for plasma surface processing. *Surface and Coatings Technology*. 1999;**116**:547-551
- [52] Slaviček P, Brablec A, Kapička V, Klíma M, Šíra M. Longitudinal emission diagnostics of plasma channel in rf barrier torch discharge. *Acta Physica Slovaca*. 2005;**55**:573-576
- [53] Janča J, Zajíčková L, Klima M, Slaviček P. Diagnostics and application of the high frequency plasma pencil. *Plasma Chemistry and Plasma Processing*. 2001;**21**(4):565-579
- [54] Novosád L, Hrdlička A, Slaviček P, Otruba V, Kanický V. Plasma pencil as an excitation source for atomic emission spectrometry. *Journal of Analytical Atomic Spectrometry*. 2012;**27**(2):305-309
- [55] Winter J, Wende K, Masur K, Iseni S, Dünnbier M, Hammer M, Tresp H, Weltmann K, Reuter S. Feed gas humidity: A vital parameter affecting a cold atmospheric-pressure plasma jet and plasma-treated human skin cells. *Journal of Physics D: Applied Physics*. 2013;**46**(29):295401
- [56] Bültner A, Lenhard U, Rahmann U, Kohse-Höinghaus K, Brockhinke A. Laskin: Efficient simulation of spectra affected by energy transfer. In: *Laser Applications to Chemical and Environmental Analysis*. p. TuE4: Optical Society of America; 2004
- [57] Yagi I, Ono R, Oda T, Takaki K. Two-dimensional lif measurements of humidity and oh density resulting from evaporated water from a wet surface in plasma for medical use. *Plasma Sources Science and Technology*. 2014;**24**(1):015002
- [58] Voráč J, Hnilica J, Kudrle V, Dvořák P. Spatially resolved measurement of hydroxyl (oh) radical concentration in a microwave plasma jet by planar laser-induced fluorescence. *Open Chemistry*. 2015;**13**(1)
- [59] Voráč J, Potočňáková L, Synek P, Hnilica J, Kudrle V. Gas mixing enhanced by power modulations in atmospheric pressure microwave plasma jet. *Plasma Sources Science and Technology*. 2016;**25**(2):025018
- [60] Voráč J, Synek P, Potočňáková L, Hnilica J, Kudrle V. Batch processing of overlapping molecular spectra as a tool for spatio-temporal diagnostics of power modulated microwave plasma jet. *Plasma Sources Science and Technology*. 2017;**26**(2):025010
- [61] Černák M, Černáková L, Hudec I, Kováčik D, Zahoranová A. Diffuse coplanar surface barrier discharge and its applications for in-line processing of low-added-value materials. *European Physical Journal Applied Physics*. 2009;**47**:22806
- [62] Černák M, Kováčik D, Ràhèl J, St'ahel P, Zahoranová A, Kubincová J, Tóth A, Černáková L. Generation of a high-density highly non-equilibrium air plasma for high-speed large-area at surface processing. *Plasma Physics Control Fusion*. 2011;**53**:124031
- [63] Kelar J, Čech J, Slaviček P. Energy efficiency of planar discharge for industrial applications. *Acta Polytechnica*. 2015;**55**:109